Clast-cortex aggregates in experimental and natural calcite-bearing fault zones

Marieke Rempe, Steven A.F. Smith, Fabio Ferri, Thomas M. Mitchell, Giulio Di Toro

PII: S0191-8141(14)00204-1
DOI: 10.1016/j.jsg.2014.09.007
Reference: SG 3123

To appear in: *Journal of Structural Geology*

Received Date: 4 June 2014
Revised Date: 5 September 2014
Accepted Date: 6 September 2014

Please cite this article as: Rempe, M., Smith, S.A.F., Ferri, F., Mitchell, T.M., Di Toro, G., Clast-cortex aggregates in experimental and natural calcite-bearing fault zones, *Journal of Structural Geology* (2014), doi: 10.1016/j.jsg.2014.09.007.

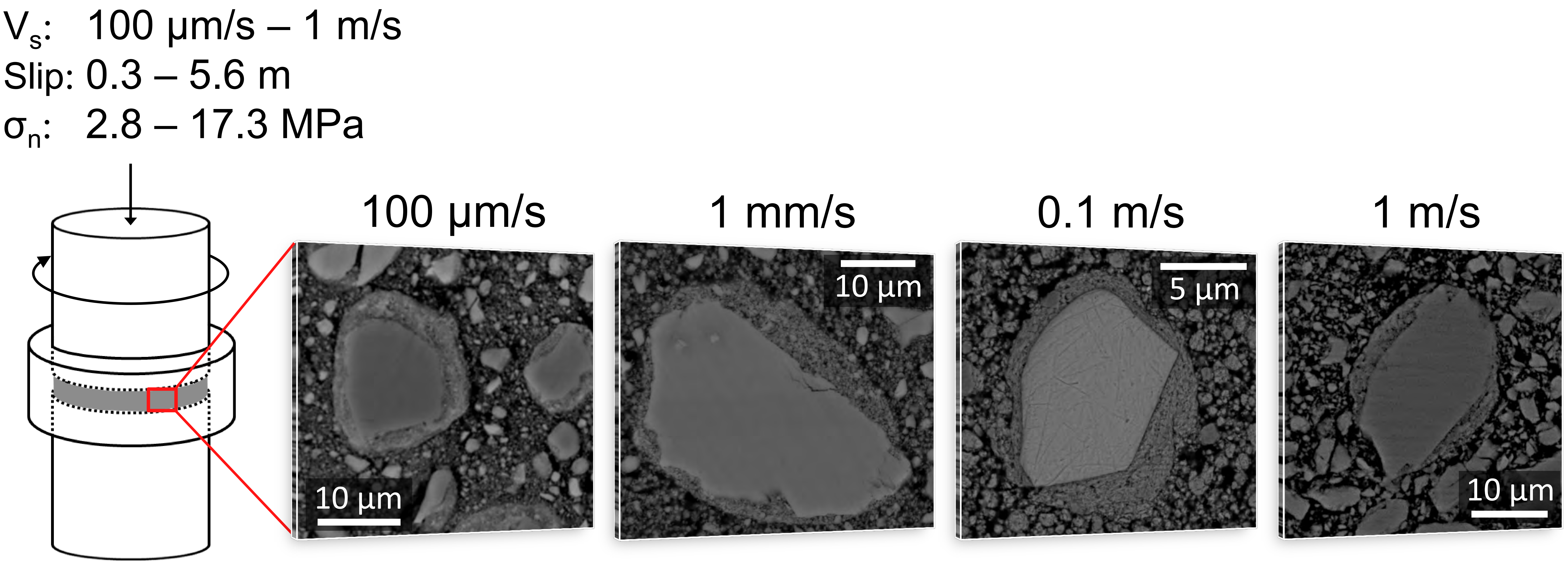

Vs: 100 µm/s – 1 m/s
Slip: 0.3 – 5.6 m
σn: 2.8 – 17.3 MPa
100 µm/s
1 mm/s
0.1 m/s
1 m/s
10 µm
10 µm
5 µm
10 µm

Clast-cortex aggregates in experimental and natural calcite-bearing fault zones

Marieke Rempe[1*], Steven A.F. Smith[2], Fabio Ferri[3], Thomas M. Mitchell[4], Giulio DI TORO[1,5]

[1]Università degli Studi di Padova
Dipartimento di Geoscienze
Via G. Gradenigo, 6
35131 Padova, PD
Italy
marieke.rempe@web.de
giulio.ditoro@unipd.it

[2]University of Otago
Department of Geology
Dunedin 9054
New Zealand
steven.smith@otago.ac.nz

[3]Universidad de los Andes
Departamento de Geociencias
Cra 1 No 18A 10 Edificio IP
Bogotá, Colombia
f.ferri@uniandes.edu.co

[4]University College London
Rock & Ice Physics Laboratory and UCL SeismoLab
Department of Earth Sciences
London, WC1E 6BT
UK
tom.mitchell@ucl.ac.uk

[5]Istituto Nazionale di Geofisica e Vulcanologia (INGV)
Via di Vigna Murata 605
Rome, Italy

*Corresponding author: marieke.rempe@web.de

Keywords: clast-cortex aggregates, CCAs, fault gouge, rotary-shear experiments, slip zones, limestone

Abstract

We investigated the formation mechanisms of rounded clast-cortex aggregates, a composite grain found in the slipping zones of faults hosted in calcite- and clay-rich rocks. The natural aggregates contain a central clast commonly made of host-rock fragments or reworked cataclasite from the slipping zone. The central clasts are surrounded by an outer cortex of calcite or clay grains a few μm or less in size. In laboratory experiments on calcite gouges using two rotary-shear apparatus we investigated the dependence of clast-cortex aggregate formation on the applied slip rate, normal stress, total displacement and ambient humidity. Clast-cortex aggregates formed at all investigated slip rates (100 μm/s to 1 m/s) but only at relatively low normal stresses (≤5 MPa). The aggregates were better developed with increasing displacement (up to 5 m) and did not form in experiments with water-dampened gouges. In the experiments, aggregates formed in low-strain regions within the gouge layers, adjacent to the highest-strain slip zones. We propose that clast-cortex aggregates in calcite-bearing slip zones form in the shallow portions of faults during shearing in relatively dry conditions, but our experiments suggest that they cannot be used as indicators of seismic slip. Formation involves clast rotation due to granular flow accompanied by accretion of fine matrix material possibly facilitated by electrostatic forces.

1. Introduction

A wide variety of micro- and meso-structural features are produced in fault zones from the interaction of deformation processes operating (often synchronously) across a range of time and length scales (e.g. Snoke et al., 1998). Recognizing (micro)structures that are characteristic of particular deformation conditions (e.g. of strain rate, total strain, fluid content) is a critical step towards interpreting fault mechanical behavior. For example, identifying seismic slip in the rock record (Cowan, 1999) relies on the identification of tectonic pseudotachylytes formed by frictional melting (Sibson, 1975; Di Toro et al., 2009), although many other fault-related structures and geochemical signatures are currently being investigated as potential seismic indicators, including, but not restricted to, injections of granular material (Lin, 1996; Smith et al., 2008; Rowe et al., 2012), pulverized fault zone rocks (Brune, 2001; Dor et al., 2006; Rempe et al., 2013), mirror-like slip surfaces (Boneh et al., 2013; Chen et al., 2013; Fondriest et al., 2013; Siman-Tov et al., 2013), localized zones of recrystallization (Kim et al., 2010; Brantut et al., 2011; Bestmann et al., 2012; Smith et al., 2013), graphitization of carbonaceous materials (Oohashi et al., 2013; Kuo et al., 2014) and thermal maturation of organic molecules (Polissar et al., 2011; Rabinowitz et al., 2013; Savage et al., 2014).

In this contribution, we focus on the conditions that determine the formation of rounded clast-cortex aggregates (CCAs; an abbreviation also used for *clay*-clast aggregates, (Boutareaud et al., 2008)), a distinctive type of composite grain recognized in several different lithologies and geological settings (Table 1). CCAs have been found in the localized slipping zones of tectonic faults (e.g. Warr and Cox, 2001; Boullier et al., 2009; Smith et al., 2011) (Figure 1) and in the basal detachment zones of large landslides (e.g. Beutner and Craven, 1996; Beutner and Gerbi, 2005; Anders et al., 2010). The main characteristic of CCAs is a central clast enclosed by an outer cortex of fine-grained material that defines the composite rounded structure (Figure 1).

Clast-cortex aggregates composed of calcite have been found in the principal slipping zone of the Tre Monti fault, an active normal fault hosted mainly in limestones in the Central Apennines of Italy (Figure 1a, b) (Smith et al., 2011). Geological constraints indicate that exposures of the principal slip zone of the Tre Monti fault were exhumed from depths of <2 km (Smith et al., 2011). The cataclastic principal slip zone (Figure 1c) consists almost entirely of calcite (from Energy Dispersive X-Ray Spectroscopy in the Scanning Electron microscope (SEM) and X-ray powder diffraction (XRD) measurements) and is up to several centimeters thick. The principal slip zone contains a texturally distinct ultracataclasite layer <10 mm thick containing CCAs between 50 μm – 3 mm diameter (Figures 1c, d). The central clasts are composed of either host-rock (fossiliferous and micritic limestone) fragments or reworked cataclasitic material (Figure 1d). The outer cortexes are up to 1 mm thick and composed of calcite with a grain size (<5 – 20 μm) similar to the surrounding matrix. The cortexes are distinguished in the petrographic microscope by a dark brown rim visible in plane-polarized light. The cortexes also contain internal color variations that often define roughly concentric laminations (Figure 1d).

Laboratory experiments can contribute to our understanding of the deformation processes resulting in the formation of CCAs. In high-velocity rotary-shear experiments on clay-bearing gouges, Boutareaud et al. (2008) and (2010) produced rounded “clay-clast aggregates” similar to those found in the most-recently active slipping zone of the Chelengpu thrust fault (1999 Mw 7.6 Chi-Chi earthquake; Boullier et al. (2009)). In the experiments of Boutareaud et al. (2008) and (2010), clay-clast aggregates were formed in both dry and water-dampened conditions, at high slip velocities (≥0.09 m/s), low normal stresses (≤1.2 MPa) and up to several tens of meters displacement. Boutareaud et al. (2008); (2010) proposed that the clay-clast aggregates were formed by dehydration of clays and subsequent thermal pressurization of pore fluids due to frictional heating, causing rotation of clasts in a liquid water/vapor medium. It was proposed that finer-grained clay materials accreted to the clasts due to electrostatic and capillary forces.

Since the initial findings of Boutareaud et al. (2008), rounded aggregates have been produced in several experimental studies (Table 1 in Han and Hirose (2012)) using clay-bearing gouges. In particular, Han and Hirose (2012) performed an experimental study on quartz and quartz-bentonite gouges. By conducting low- to high-velocity rotary-shear experiments, Han and Hirose (2012) found that clay-clast aggregates developed in their experiments at both sub-seismic and seismic sliding velocities (500 µm/s – 1.3 m/s) and only under room-dry conditions. The results of Han and Hirose (2012) suggest that rounded aggregate grains may not be a reliable indicator of fast slip in clay-bearing gouges, and that the mechanisms leading to the formation of aggregate grains warrant further study.

In this study, rotary-shear experiments were conducted on layers of synthetic calcite gouge to investigate the processes contributing to the formation of natural and experimental CCAs in calcite-bearing slip zones like the Tre Monti normal fault (Smith et al., 2011). We systematically studied not only the dependence on slip velocity, on which Boutareaud et al. (2008) and Han and Hirose (2012) concentrated, but also the effect of total displacement, normal stress, and ambient humidity (i.e. room-dry, water-dampened and vacuum). Our results contribute to a better understanding of the significance of CCAs in tectonic fault zones, and provide constraints on the deformation processes active within shallow, granular slipping zones in carbonates.

2. Methods

2.1. *Experimental Set-Up*

A total of thirty-six rotary-shear experiments were conducted using two rotary-shear apparatus at normal stresses ranging from 1 to 17 MPa, slip rates over four orders of magnitude (0.0001 to 1 m/s) and total displacements from 0.27 to 5.58 m under both room-dry and water-dampened conditions (Table 2). Twenty-two experiments were performed at low normal stresses (1 to 3 MPa) with ROSA (**Ro**tary-**S**hear **A**pparatus) installed at the Department of Geosciences of Padua University (Padua, Italy). Fourteen experiments were performed at higher normal stresses (2.8 – 17.3 MPa) with SHIVA (**S**low- to **HI**gh-**V**elocity **A**pparatus) installed at the Istituto Nazionale di Geofisica e Vulcanologia (INGV) in Rome, Italy. SHIVA was also used to perform three additional experiments under vacuum (10^{-4} mbar) conditions.

Due to the circular sample geometry used in the rotary-shear configuration, slip velocity and total displacement depend on the position along the radius of the sample. Thus, we follow Hirose and Shimamoto (2005) and calculate an "equivalent velocity" $v_e = \frac{4\pi R(r_i^2+r_ir_o+r_o^2)}{3(r_i+r_o)}$, with r_i and r_o being the inner and outer radius of the sample, respectively, and R the number of revolutions per minute. The total displacement consequently corresponds to the equivalent displacement $d_e = v_e t$.

2.1.1. Experiments with ROSA

The basic set-up of ROSA, built by MARUI & CO., LTD (model MIS-233-1-77) as designed by T. Shimamoto, is illustrated in Figure 2a. It has a 11 kW servomotor with revolving speeds from 1.5 rpm to 1500 rpm, which can be reduced by a factor of up to 10^{-6} by a gear system. The revolution speed is measured via a rotary encoder (Figure 2a, R1; 3600 pulses/revolution). The torque is measured by averaging the output from two compression load cells (Figure 2a, T1 and T2) with a resolution of 0.5 N. To obtain information about shortening and dilation of the samples, the axial displacement is measured with a high-sensitivity displacement gauge (Figure 2a, D) with a resolution of 1 μm. A normal load of up to 10 kN can be applied on the stationary column via a pneumatic system; for higher normal stresses of up to 50 kN a hydraulic cylinder can be installed. The applied load is monitored by a compression load cell (Figure 2a, L) with a resolution of 5 or 25 N for the pneumatic and hydraulic cylinders, respectively. Mechanical data are collected at a rate of up to 1 kHz.

Of the twenty-two gouge experiments conducted with ROSA (Table 2), fourteen were performed by sandwiching a layer of gouge up to a few millimeters thick between two solid rock cylinders 25 mm in diameter (typically tonalite or gabbro). The surfaces of the solid rock cylinders were roughened with 150 grit to promote deformation within the gouge layer. The gouges were contained along the outside by a Teflon sleeve fastened with a jubilee clip (Figure 2b). Several tests run to measure the friction of the Teflon sleeve showed that it contributes approximately 10-15% (corresponding to $0.05<\mu<0.1$) to the measured friction values (where the friction coefficient, μ, is calculated as shear stress/normal stress). This is consistent with the findings of Sawai et al. (2012) who reviewed the influence of Teflon friction in ten high-velocity experimental studies that employed a similar sample geometry. We have chosen not to correct the mechanical data for the effects of Teflon friction. The sample assembly is fixed in the apparatus with hydraulic-mechanical locks. Rotation of the upper column shears the gouge layer. After the experiment, the entire sample assembly (solid rock cylinders + gouge layer + Teflon ring + jubilee clip) can be impregnated with epoxy resin thus minimizing gouge loss and potential disruption of microstructures. Eight experiments were conducted using an annular steel sample holder (Figure 2c). In this setup, the ring-shaped gouge layer (with int./ext. diameters of 25/40 mm) is contained by inner and outer Teflon rings.

2.1.2. Experiments with SHIVA

A detailed report of the design and capabilities of SHIVA is provided in Di Toro et al. (2010). With SHIVA, an annular steel gouge sample holder was used (description and calibration tests in Smith et al. (2013)). Inner and outer rings contain the gouge layer (int./ext. diameters of 35 and 55 mm) and slide over a base disc (Figure 2d). Using an all-steel gouge holder prevents contamination of the gouge sample by decomposition of Teflon. Mechanical data are collected at a rate of up to 25 kHz. SHIVA is equipped with a Pfeiffer Hi cube vacuum pump that is able to create a minimum pressure of 10^{-4} mbar in a chamber surrounding the samples (described in Violay et al. (2013)). During an experiment in near-vacuum conditions, this pre-imposed pressure might increase due to the release of volatiles from the gouge sample, in our case due to thermal decomposition of calcite.

2.2. Sample Preparation and Analysis Techniques

The gouge experiments were conducted on powder derived from Carrara marble (Figure 3a). The marble was first ground to a powder in a pestle and mortar for several minutes and then sieved to different particle size fractions. For the starting materials, the fractions <150 µm and <180 µm were used in, respectively, Padua and Rome. The single fractions were weighted to obtain the particle-size distribution of the starting material (Figure 3b). Three batches of starting material (CMG1, 2 and 3) were prepared consecutively, two of which were analyzed using semi-quantitative X-ray powder diffraction at the Geoscience Department, University of Padua (Figure 3c). The software package High Score Plus (PANalytical) was used for phase identification and quantitative phase analysis by the Rietveld method (Rietveld, 1967). Batch CMG2 is composed of c. 72.3% magnesium calcite, 21.7% dolomite, and 6% white mica (muscovite/illite). Batch CMG3 is composed of >98% calcite and <2% white mica. SEM analysis indicates that the composition of CGM1 is similar to that of CMG3, containing only minor amounts (<2%) of dolomite and white mica.

For experiments with ROSA, 1.5 g of starting material was used to produce a pre-experiment gouge layer thickness of c. 1.5 mm. For SHIVA, 5 g of starting material were used to produce a gouge layer thickness of c. 3 mm. When water-dampened gouge was used, 20 wt% deionized H_2O was evenly added to the gouge layer using a syringe.

After each experiment the deformed gouge sample was saved in epoxy, and polished petrographic sections were prepared for microstructural analysis. The sections were cut approximately parallel to the slip direction and perpendicular to gouge layer boundaries. Samples were analyzed using a JEOL JSM-6500F Field-Emission Scanning Electron Microscope (SEM) in backscattered mode (acceleration voltage 20 kV; working distance 8 - 20 mm) at the Istituto Nazionale di Geofisica e Vulcanologia (INGV) in Rome. SEM images of selected samples were used to investigate grain size and shape characteristics using the image analysis software Fiji (Schindelin et al., 2012).

3. Results

3.1. Mechanical Behavior of Calcite Gouges

The friction coefficient (μ; shear stress/normal stress) in both room-dry (Figure 4a) and water-dampened (Figure 4b) experiments ranges from 0.5 to 0.8. In experiments at high-velocity (>1 m/s) and high normal stress (>10 MPa), initial peak friction of c. 0.8 was observed after 0.1-0.2 m of slip (e.g. s272 in Figure 4a). In such cases, peak friction was followed by dynamic weakening that reduced the friction coefficient to a "steady-state" value between 0.3-0.6.

All experiments conducted with room-dry and water-dampened gouges showed initial gouge compaction of 100 – 300 μm (Figures 4a, b). In some room-dry experiments, a transient phase of dilation occurred following initial compaction (e.g. s272, Figure 4a). When observed, this transient dilation was between 10 – 30 μm and was followed by renewed compaction (e.g. 272, Figure 4a). In some experiments, a second phase of dilation was recorded after displacements >0.5 m (e.g. s776 in Figure 4a). In those cases, secondary dilation was between 5 – 180 μm, but may include a component that reflects minor gouge loss (in the experiments performed with ROSA). Figure 5 summarizes measurements of transient dilation and total dilation (i.e. transient + secondary dilation). In room-dry experiments, the amount of secondary dilation tends to increase with displacement. No significant amount of gouge layer dilation was recorded at any stage during experiments with water-dampened gouges (Figure 5).

3.2. Strain localization and textural zones in room-dry experiments

Up to three distinct microstructural zones are present within the deformed room-dry samples (Figure 6a):

1. Zone I consists of relatively coarse-grained gouge similar to the starting material. In zone I, grains are angular to sub-angular and up to c. 150 μm in size.
2. Zone II is up to 800 μm thick and has a compacted and highly comminuted matrix with grain sizes on the order of a few microns (Figures 6a, b). The matrix contains larger grains up to 100 μm in size composed of a central clast surrounded by a fine-grained outer cortex defining an overall rounded shape, i.e. calcite CCAs (Figure 6b-d). In all of the

experimental samples that were analyzed with the SEM, Zone II is the only zone in which CCAs were developed. The central clasts often contain angular embayments along their outer margins that are in-filled by finer cortex material (Figure 6c). Calcite grains comprising the cortex are <1 μm in size and appear to be loosely aggregated (Figure 6d). Individual rounded grains on the order of 100 nm in size are recognizable.

3. Zone III is up to 300 μm thick and comprises highly comminuted and banded gouge material (Figures 6a, e). The banding is wavy and defined by variations in grain size and porosity (Figure 6e). Internally, single bands up to 100 μm wide contain grain size grading, with finer-grained material towards the stationary side. The stationary side of each band is typically marked by a discrete fracture surface that may have originated as a shear surface in the experiments.

The distribution of the three zones depends on experimental conditions, and not all three zones are always present. In experiments with relatively high displacements or high slip velocities (e.g. r88 in Figure 6a), zones II and III are well developed at the expense of zone I. Zones II and III are typically best developed at a distance of a few millimeters from the outer edge of the cylindrical samples (Figure 6a), before they thin again towards the outer edge where slip velocity and total displacement were highest (Figure 6a). Within zone II, CCAs formed preferentially in areas with relatively high porosity (e.g. Figure 6b). In some samples, a thin sliver (<100 μm) of comminuted material belonging to zone II is variably developed adjacent to the stationary side of the gouge holder (Figure 6a), although this sliver does not contain CCAs.

3.3. Strain distribution in room-dry experiments

Figure 7 shows the microstructure of an experiment (s886) containing a c. 2 mm-wide strain marker made from dolomite gouge (particle size <250 µm). The vertical marker was constructed perpendicular to gouge layer boundaries and the imposed shear direction, allowing the angular strain (γ) within the deformed gouge layer to be calculated as $\gamma = \tan\phi$, where ϕ is the angle between the original and deformed marker (Figure 7a). In this experiment, the margins of the marker were not sheared to the same degree (Figure 7b), which may be due to the thickness of the marker and the annular geometry of the sample. For the evaluation of shear strain an average of the angles as shown in Figure 7b was taken. Towards the rotary side of the gouge layer, the marker is only slightly distorted, defining a zone of low strain (mean $\gamma \leq 1.6$). Further towards the stationary side of the gouge layer, the marker is sheared progressively towards parallelism with the gouge layer boundaries, defining an intermediate-strain domain (mean $\gamma \geq 3.1$). In a layer c. 220 µm thick adjacent to the stationary-side, the marker is heavily disrupted, but some individual dolomite grains are dispersed throughout this layer. Assuming that almost all of the total displacement was accommodated in this layer (only a negligible amount of displacement is accommodated in the low- and intermediate-strain domains where the dolomite marker remains intact), the bulk strain can be approximated by dividing its thickness (220 µm) by the total experimental displacement of 2.5 m, resulting in a finite shear strain of c. 1850.

Several R1-Riedel shears (terminology after e.g. Logan et al., 1979), defined by bands of grain-size reduction and fractures (the latter assumed to have formed by normal stress unloading), cut through the low- and intermediate-strain domains at angles of c. 15-20° to the gouge layer boundaries (yellow dashed lines in Figure 7b). Where the R1-shears cut the dolomite marker, discrete offsets of c. 10-180 µm are observed along the margins of the marker, with the sense of offset systematically the same as the bulk shear sense (i.e. synthetic R1-shears). The fine-grained high-strain layer is also cut by fractures that link downwards into the R1-shears. These fractures are characteristically observed in the highest-strain layers at the end of experiments and are thought to have formed by normal stress unloading at the end of the experiments.

3.4. Formation Conditions of Experimental Clast-Cortex Aggregates

As noted above, CCAs formed exclusively within Zone II in the deformed gouges. In addition, they were formed only under certain experimental conditions. In Figure 8, experiments performed over a wide range of normal stresses, slip velocities and displacements are classified as having mainly well-developed (W), poorly-developed (P) or no (N) CCAs. Red letters indicate room-dry experiments and blue letters indicate water-dampened experiments. Well-developed CCAs are those with a cortex that completely surrounds the central clast, defining an overall rounded structure (e.g. Figure 8d). Poorly-developed CCAs are those where the cortex does not completely surround the central clast (e.g. Figure 8e).

3.4.1. Room-dry Conditions

Figure 8a shows the dependence of CCA formation on slip velocity and displacement at 1 and 3 MPa normal stress under room-dry conditions (red letters). At 1 MPa normal stress CCAs are generally well developed (e.g. example in Figure 8d), except in experiments that have low velocity (<0.1 m/s) combined with low total displacement (0.5 m). At higher displacements (>3 m), aggregates form at all investigated slip velocities. At a higher normal stress of 3 MPa, longer displacements are needed to form aggregates: At 3 MPa, no CCAs developed in experiments with 0.5 m displacement and well-developed CCAs only formed in experiments with displacements of more than c. 4 m.

The effect of normal stress on the formation of CCAs was further tested by carrying out a separate series of five experiments over a wider range of normal stresses than shown in Figure 8a, at a constant slip velocity of 0.1 m/s and a total displacement of 3 m (Figure 8b). These experiments show that for a given layer thickness, CCAs are better developed at lower normal stresses. With a 3 mm thick starting gouge layer, CCAs were not developed at a normal stress of 17 MPa, poorly developed at 10 MPa, and well developed at 5 MPa. With a 1.5 mm thick gouge layer, CCAs were poorly developed at 3 MPa and well developed at 1 MPa. These data indicate that in room-dry calcite gouges CCAs are preferentially formed at relatively low normal stress.

3.4.2. Wet Conditions

No CCAs developed under wet conditions (Figure 8a, blue letters), regardless of the slip velocity or total displacement. The microstructure of the wet samples (Figure 9) is characterized by a relatively thick zone adjacent to the rotary side which contains large rounded to sub-rounded grains embedded in a uniformly fine-grained matrix (grain size <20 µm).

3.4.3. Vacuum Conditions

Three experiments with SHIVA were conducted under vacuum conditions (i.e., at 10^{-4} mbar) at 0.1 m/s, 3 m total displacement and normal stresses of 3, 5 and 10 MPa (Figure 8c). In the samples from the 3 and 10 MPa experiments the three characteristic microstructural zones were not observed and no CCAs were found, but this may be due to poor sample preservation. Poorly-developed CCAs formed at 5 MPa normal stress.

3.5. Size and Shape Analysis of Clast-Cortex Aggregates

Two-dimensional image analysis (Fiji software, Schindelin et al., 2012) was used to calculate two shape factors for the central clasts and outer cortexes of the CCAs; the circularity and the solidity (Heilbronner and Barrett, 2013). The circularity is defined as $C = 4\pi \frac{A}{P^2}$ where *A* is the area and *p* the perimeter of the central clast or outer cortex (Figure 10a). A circularity of $C = 1$ describes a perfect circle. The solidity is the ratio between the area of the object and the convex area $S = \frac{A}{A_{convex}}$ (Figure 10a), so that a structure with no embayments yields $S = 1$.

SEM backscatter images (for the experimental samples; Figure 10b) or optical photomicrographs (for the natural samples; Figure 10c) were used to trace the outlines of central clasts and outer cortexes. For the experimental example, a representative SEM image from sample r80 was evaluated (Figure 10b). The area covered by the image was 190 µm x 240 µm and contained 45 CCAs (Figure 10b). For the natural example, the optical photomicrographs used to trace the CCAs covered an area of approximately 24 mm x 5.4 mm and contained 137 CCAs (Figure 10c). Circularity and solidity were calculated separately for 1) experimental central clasts, 2) experimental cortexes (i.e. the outer margins of the CCAs), 3) natural central clasts, and 4) natural cortexes. The frequency of a certain circularity or solidity value was then plotted using bin sizes of 0.1 and 0.025, respectively (Figure 11).

The results in Figure 11a show that the cortexes are more circular than the central clasts in both natural and experimental cases. The experimental cortexes have a notably higher mean circularity ($C_{mean} = 0.761$) than the experimental central clasts ($C_{mean} = 0.696$). The natural cortexes have a mean circularity of 0.81 whereas the natural central clasts have a mean circularity of 0.764. Additionally, the data indicate that natural cortexes and central clasts are more rounded on average than their experimental counterparts.

The solidity values (Figure 11b) show the same overall results. In both natural and experimental samples, the cortexes have a higher mean solidity than the central clasts, suggesting that the fine-grained material comprising the cortexes fills embayments within the central clasts, consistent with microstructural observations. This effect is most pronounced in the experimental samples, where the solidity values for the outer cortexes are notably higher (S_{mean} = 0.943) than for the central clasts (S_{mean} = 0.905).

4. Discussion

4.1. Development of the textural zones

The development of distinct textural zones is a common feature in rotary-shear gouge experiments (e.g. Beeler et al., 1996; Kitajima et al., 2010). In this study, the distribution of textural zones I, II and III depends both on experimental conditions and the radial position within the gouge layer. Zones II and III generally become thicker towards the margins of the cylindrical samples where slip velocity and displacement are higher, but then become thinner again close to the outer margins (Figure 6a). This effect has previously been described by Beeler et al. (1996) who attributed it to the friction of the moving gouge material against the outer containment ring (Teflon in the their case) reducing the degree of deformation close to the border. We observed a similar effect in our gouge experiments where the deforming gouge was in contact with the outer steel ring (in SHIVA) or Teflon ring (in ROSA) (Figure 2d).

The strain-marker experiment indicates that the highly-comminuted material in zone III represents the principal slip layer where most of the strain was localized. The banded appearance of the gouge in this layer, and the grain size grading within individual bands, is comparable to that reported by other authors, e.g. Kitajima et al. (2010) and Yao et al. (2013). Yao et al. (2013) observed that the finest material (<1 μm) within these bands was welded or sintered, a process likely caused by the localization of slip and subsequent frictional heating in the localized zone (Lachenbruch, 1980; Rempel and Rice, 2006; Platt et al., 2014). As suggested by Shimamoto and Togo (2012), the welding of grains may act to strengthen the slip zone and cause deformation within it to "migrate" to an adjacent area, resulting in multiple bands within a localized zone of high strain.

4.2. Comparison of natural and experimental CCAs

The CCAs found in the experimental and natural samples are similar in structure and shape. This is confirmed by quantitative analysis of two shape factors (circularity and solidity). In both experiment and nature, the central clasts are generally more angular than the outer cortexes (see Figure 1 and 8). Natural CCAs have higher circularities and solidities than their experimental counterparts. This may be due to the natural central clasts and outer cortexes having experienced multiple slip episodes (and hence more comminution and abrasion), as opposed to the single slip episodes represented by the experiments. The size of the experimental CCAs is limited by the maximum particle size used in the experiments (180 μm) and, possibly, by the layer thickness (1.5 or 3 mm). The natural CCAs are up to 3 mm in size, and confined to an ultracataclastic slipping zone up to c. 2 cm thick.

In both experiment and nature, the aggregates sometimes consist of clustered matrix material rather than single host rock grains with a cortex. In the natural examples, the clustered material is typically reworked cataclasite that can contain relatively large angular grains within a finer matrix (Figure 1d). In the case of the experiments, the material clusters are likely to be fragments of fine-grained material from the high-strain zones (Figure 12a).

The cortex of fine-grained calcite in the natural examples ranges in thickness from ≤10 µm to c. 500 µm. In some samples from the natural slipping zones, outer cortexes surround almost all host rock fragments larger than c. 100 µm. In many cases, the natural cortexes are laminated (Figure 1b) and, infrequently, grain size grading within the cortex material is observed, with slightly larger grains towards the inside of individual cortex laminations (Smith et al., 2011). In the experimental samples, the maximum thickness of the outer cortex is on the order of 15 µm, and multiple laminations are observed in some samples (Figure 12b).

It was proposed by Boutareaud et al. (2008) and (2010), in the case of clay-bearing aggregates, that the central clasts accreted fine-grained material from the surrounding matrix. They further suggested that the aggregation process was controlled by electrostatic charges (due to the electrical double layer at the surface of the clay particles and a triboelectric effect) and that thermal pressurization of the gouge layers played a significant role. The triboelectric effect is responsible for electrostatic charging of particles due to frictional contact (Matsusaka et al. (2010), and references therein). Thermal pressurization creates dilation that is thought to provide additional space for grain rolling and accretion of fine material (Boutareaud et al., 2010).

There is no microstructural evidence for crystal-plastic processes (e.g. sutured or sintered grains, lobate grain boundaries) in any of the experimental CCAs we studied. High-resolution SEM images of our experimental CCAs show that the grains in the cortexes (<500 nm) appear loosely aggregated (Figure 6d). Most of the grains are angular or sub-angular, with only the smallest grains (<500 nm) having a rounded shape.

CCAs only formed in our room-dry and vacuum experiments, in which total dilation was up to 180 µm. Additionally, *well*-developed CCAs were favored at large displacements, in experiments that had relatively large amounts of secondary dilation. In wet experiments, CCAs did not form and dilation was not measured at any stage. Following Han and Hirose (2012) and Boutareaud et al (2008, 2010), we suggest that the CCAs in our experiments formed by rolling of the central clasts facilitated by shear dilatancy, and that this provided the frictional contacts resulting in electrostatic charging of the smaller matrix particles. If thermal pressurization contributed to (secondary) layer dilation at larger displacements, it may be an important process in the formation of well-developed CCAs.

4.3. Deformation conditions necessary to form experimental CCAs

4.3.1. The role of displacement and strain

CCAs were better developed in our experiments at displacements exceeding 0.5 m. Significantly, they only formed in the intermediate-strain zone (Zone II) in the samples, suggesting that there is an upper and lower strain limit for their formation. This is consistent with previous experimental studies that typically show CCAs developing outside the zone of highest strain (e.g. Boutareaud et al., 2008; Kitajima et al., 2010; Han and Hirose, 2012). The strain-marker experiment reported here, combined with ongoing work on additional strain-marker experiments (Di Toro et al., 2013), suggests that CCAs developed in the experimental calcite gouges at relatively low strains on the order of $2 \le \gamma \le 14$.

The upper bound for strain ($\gamma = 14$) in the CCA-bearing Zone II results from strain localizing in Zone III. After localization has been achieved, a bulk of the displacement is hosted in the high-strain layer (Zone III), limiting strain accumulation in the CCA-bearing Zone II. Under the normal stress conditions investigated in these experiments, strain localization in 1.5 – 3 mm thick calcite gouge layers typically occurs in the first few tens of centimeters of displacement (Smith et al., 2012). However, CCAs were well developed in these experiments for displacements >0.5 m. This suggests that CCAs form and continue to evolve after localization has occurred, indicating that there must be ongoing shearing in Zone II (and possibly Zone I) of the samples throughout the experiments. This also explains the occurrence in Zone II of reworked fragments of fine-grained Zone III material.

4.3.2. The role of slip velocity

In the experiments, CCAs formed independently of the applied slip velocity, which covered four orders of magnitude (from 100 μm/s to 1 m/s). These results suggest that CCAs found in the slipping zones of calcite-bearing faults in nature are not unequivocal evidence for seismic slip. This is in agreement with the results of Han and Hirose (2012) for quartz and quartz-bentonite gouges, who found that clay-clast aggregates formed in low-velocity (0.0005 m/s) rotary-shear experiments.

When interpreting the experimental microstructures, it is important to consider the strong velocity gradient across the thickness of the gouge layer. Like strain, the strain *rate* in Zone III will be much higher, while the bulk of the gouge (Zones I and II) experiences much lower strain rates. Assuming that the different strain domains started to develop at the onset of the experiments and were sheared at a constant rate, we can roughly calculate the strain rate in each zone as maximum slip velocity / zone thickness. For the strain-marker experiment s886 we find that the strain rates in Zones I, II and III were approximately 0.64 s^{-1}, 1.2 s^{-1} and 740 s^{-1}, respectively, indicating that the strain rate in Zone III was more than two orders of magnitude higher than in the other zones. The values for Zones II and III likely represent lower limits because those zones probably started to develop later than Zone I.

The natural calcite CCAs from the Tre Monti fault are sharply truncated in some cases by discrete principal slip surfaces (Figure 12 in Smith et al., 2011). Similar truncated clasts associated with discrete "mirror-like" slip surfaces in dolomite gouges were produced in experiments at seismic slip velocities (Fondriest et al., 2013). If the conclusions of Fondriest et al. (2013) are also applicable to calcite gouges, the occurrence of truncated CCAs in the Tre Monti fault suggests that it experienced seismic slip, even if the CCAs themselves may have formed at lower slip velocities.

4.3.3. The role of normal stress

Normal stress plays a crucial role in the formation of experimental CCAs. Well-developed CCAs were only found in experiments at normal stresses ≤5 MPa, although the normal stress at which CCAs form also depends on the gouge layer thickness (Figure 8b). Possible factors preventing formation of CCAs at higher normal stresses are 1) faster strain localization (Smith et al., 2012) and 2) increased compaction at higher normal stresses. In the first instance, faster localization of strain to a narrow high-strain zone may result in the bulk of the gouge layer experiencing strain of $\gamma<2$, below the lower bound necessary to form CCAs under the investigated conditions. In the second instance, greater compaction and hence reduction of porosity in the gouge matrix might restrict rolling of clasts to such a degree that the outer cortexes do not form.

Although gouge zone thickness along natural faults is highly variable, compilations of geological and geophysical data pertaining to the thickness of the coseismic slip zone in the brittle crust suggest typical layer thicknesses on the order of several millimeters to a few centimeters (Sibson, 2003), comparable to the layer thicknesses used in our experiments. Our results suggest that in nature the formation of CCAs may be restricted to relatively shallow crustal levels. This is broadly compatible with existing case studies reporting CCAs in natural slipping zones, which all come from fault zones exhumed from relatively shallow crustal depths (<4 km; Table 1). For example, in the Tre Monti fault (Smith et al., 2011), the

CCA-bearing cataclastic slip zone directly underlying the principal slip surface is 2 to 10 mm thick and exhumed from a depth of <2 km. In cores from borehole A drilled through the Chelungpu thrust fault, clay-clast aggregates were found in the 2-3 cm thick principal slip zone of the 1999 Chi-Chi earthquake located at depths of c. 1.11-1.14 km (Boullier et al., 2009). Interestingly, in borehole B, where the principal slip zone is much thinner (c. 0.3 cm) CCAs were only found in gouge material flanking the principal slip zone (Boullier et al., 2009). Based on our experiments, this may be because the strain in the thin principal slip zone itself was higher than that required for CCA formation.

4.3.4. Ambient Conditions

No CCAs developed in the experiments with water-dampened calcite gouges. In studies on the charging characteristics of various materials it was shown (Greason, 2000; Nomura et al., 2003) that the net charge due to triboelectrification (in the order of 10^{-8} Coulomb) generally decreased with increasing humidity. If this is applicable to charging induced by friction of calcite grains against each other, or against the steel and Teflon walls of the gouge holders, the reduced triboelectric force due to the high (~20 wt%) water content of the gouge could be too low to attract the fine material to the larger clasts. Due to the higher permittivity in a water-saturated gouge as compared to room-humid gouge (Hector and Schultz, 1936; Chistyakov, 2007), the electrostatic Coulomb force acting between the particles will also be reduced.

In addition, the presence of water causes faster slip localization, reducing the strain accommodated in the bulk gouge layer outside the principal slip zone (Faulkner et al., 2010; Ferri et al., 2010). Dilation of the gouge layers was almost never observed in wet experiments. Faster slip localization combined with rapid compaction of the gouge layer are likely to restrict grain rolling, and thus the formation of CCAs, in the water-dampened gouges.

Our results showing that CCAs did not form in water-dampened gouges are consistent with the experiments on clay-bearing gouges by Han and Hirose (2012) and Ferri et al. (2011), but contrast the results of Boutareaud et al. (2008), (2010). The latter authors found that clay-clast aggregates developed in clay-bearing gouge samples that were initially saturated with water. However, as noted by Han and Hirose (2012), the total displacements in the experiments by Boutareaud et al. (2008), (2010) were up to 64 m. Due to frictional heating at such large displacements, the temperatures in the experiments of Boutareaud et al. (2008), (2010) increased to c. 200°C in the center and c. 400°C at the periphery of the samples. This may have resulted in evaporation of the water, resulting in effectively dry conditions after displacements of a few meters.

According to the experiments performed in this study, the formation of CCAs is favored by relatively dry conditions. Smith et al. (2011) found evidence of layer fluidization and syn-tectonic vein formation in the CCA-bearing principal slip zone of the Tre Monti fault, suggesting fluid involvement in faulting. The same is true for the slipping zones of the Chi-Chi earthquake (Boullier et al., 2009), where there is evidence of gouge layer fluidization. This raises two possibilities that warrant further investigation; the first is that fluidization processes (that cannot be effectively investigated in the present gouge experiments) play a role in the formation of CCAs in nature. The second is that fluid availability in natural slipping zones is highly variable in time (e.g. during the seismic cycle) and space (e.g. due to fault geometry), with the natural CCAs forming during restricted time intervals in relatively dry parts of the slipping zones.

5. Conclusions

We investigated the conditions necessary to form clast-cortex aggregates (CCAs) in granular calcite gouges by performing low- to high-velocity experiments in a rotary-shear configuration. The experimental results show that in calcite gouges CCAs are well developed at displacements >0.5 m, normal stresses ≤5 MPa, and in room-dry or vacuum conditions. Significantly, CCAs developed at all investigated slip rates (0.001 m/s to 1 m/s), spanning the subseismic to seismic range. No CCAs formed in water-dampened gouges.

Experimental CCAs were formed in relatively low-strain domains outside the principal slipping zones, where the bulk shear strain was between 2 and 14. Analysis of the circularity and solidity of the experimental CCAs as well as of natural examples from the calcite-dominated principal slip zone of the Tre Monti normal fault in Italy, indicates that experimental and natural examples have similar microstructural characteristics and grain shapes. We suggest that CCAs in calcite gouges form by grain rolling associated with shear dilatancy, accompanied by progressive accretion of fine-grained matrix material. The interface-scale mechanisms leading to accretion of fine-grained matrix material in the cortexes require further investigation by higher-resolution methods.

Overall, our results suggest that CCAs in calcite-bearing slipping zones likely form in shallow and (at least locally) fluid-poor fault environments, in granular layers flanking the highest-strain ultracataclasites. In experiments, CCAs form in calcite gouges over a range of subseismic to seismic slip rates, suggesting that in natural slipping zones they cannot be used as a reliable indicator of seismic slip.

6. Acknowledgements

The authors would like to thank Michele Fondriest, Silvia Mittempergher, Stefan Nielsen, Nicola Praticelli and Marie Violay for technical assistance, Leonardo Tauro for help with the sample preparation, Luca Perruzo, Andrea Cavallo and Rolf Neuser for support with the SEM and Federico Zorzi for XRD analyses. Anne-Marie Boullier and Raehee Han are thanked for constructive comments. MR acknowledges funding by Ca.Ri.Pa.Ro., SAFS acknowledges funding from a 2014 University of Otago Research Grant. GDT acknowledges the European Research Council Starting Grant ''USEMS'' (no. 205175).

7. References

Anders, M. H., E. Aharonov, et al. (2000). "Stratified granular media beneath large slide blocks: Implications for mode of emplacement." Geology **28**(11): 971-974.

Anders, M. H., B. W. Fouke, et al. (2010). "The Role of Calcining and Basal Fluidization in the Long Runout of Carbonate Slides: An Example from the Heart Mountain Slide Block, Wyoming and Montana, U.S.A." The Journal of Geology **118**: p. 577-599.

Beeler, N., T. Tullis, et al. (1996). "Frictional behavior of large displacement experimental faults." Journal of Geophysical Research: Solid Earth (1978–2012) **101**(B4): 8697-8715.

Bestmann, M., G. Pennacchioni, et al. (2012). "Deformation and ultrafine dynamic recrystallization of quartz in pseudotachylyte-bearing brittle faults: A matter of a few seconds." Journal of Structural Geology **38**: 21-38.

Beutner, E. C. and A. E. Craven (1996). "Volcanic fluidization and the Heart Mountain detachment, Wyoming." Geology **24**(7): 595-598.

Beutner, E. C. and G. P. Gerbi (2005). "Catastrophic emplacement of the heart mountain block slide, Wyoming and Montana, USA." Geological Society of America Bulletin **117**(5-6): 724-735.

Boneh, Y., A. Sagy, et al. (2013). "Frictional strength and wear-rate of carbonate faults during high-velocity, steady-state sliding." Earth and Planetary Science Letters **381**(0): 127-137.

Boullier, A. M., E. C. Yeh, et al. (2009). "Microscale anatomy of the 1999 Chi-Chi earthquake fault zone." Geochemistry Geophysics Geosystems **10**.

Boutareaud, S., A. M. Boullier, et al. (2010). "Clay clast aggregates in gouges: New textural evidence for seismic faulting." Journal of Geophysical Research-Solid Earth **115**.

Boutareaud, S., D. G. Calugaru, et al. (2008). "Clay-clast aggregates: A new textural evidence for seismic fault sliding?" Geophysical Research Letters **35**(5).

Boyer, S. E. and J. R. Hossack (1992). "Structural features and emplacement of surficial gravity-slide sheets, northern Idaho-Wyoming thrust belt." Regional Geology of Eastern Idaho and Western Wyoming **179**: 197.

Brantut, N., R. Han, et al. (2011). "Fast slip with inhibited temperature rise due to mineral dehydration: Evidence from experiments on gypsum." Geology **39**(1): 59-62.

Brune, J. (2001). "Fault normal dynamic loading and unloading: an explanation for ‘‘non-gouge’’rock powder and lack of fault-parallel shear bands along the San Andreas fault." EOS Trans. Am. Geophys. Union **82**: 47.

Chen, X., A. S. Madden, et al. (2013). "Dynamic weakening by nanoscale smoothing during high-velocity fault slip." Geology **41**(7): 739-742.

Chistyakov, A. D. (2007). "The permittivity of water and water vapor in saturation states." Russian Journal of Physical Chemistry A **81**(1): 5-8.

Cowan, D. S. (1999). "Do faults preserve a record of seismic slip? A field geologist's opinion." Journal of Structural Geology **21**(8): 995-1001.

Di Toro, G., A. Niemeijer, et al. (2010). "From field geology to earthquake simulation: a new state-of-the-art tool to investigate rock friction during the seismic cycle (SHIVA)." RENDICONTI LINCEI **21**(1): 95-114.

Di Toro, G., G. Pennacchioni, et al. (2009). "Pseudotachylytes and earthquake source mechanics." International geophysics **94**: 87-133.

Di Toro, G., M. Rempe, et al. (2013). "Strain localization in experimentally sheared gouge layers." Abstract MR13A-2258 presented at 2013 Fall Meeting, AGU, San Francisco, Calif., 9-13 Dec.

Dor, O., Y. Ben-Zion, et al. (2006). "Pulverized rocks in the Mojave section of the San Andreas Fault Zone." Earth and Planetary Science Letters **245**(3-4): 642-654.

Faulkner, D. R., C. A. L. Jackson, et al. (2010). "A review of recent developments concerning the structure, mechanics and fluid flow properties of fault zones." Journal of Structural Geology **32**(11): 1557-1575.

Ferri, F., G. Di Toro, et al. (2011). "Low- to high-velocity frictional properties of the clay-rich gouges from the slipping zone of the 1963 Vaiont slide, northern Italy." Journal of Geophysical Research-Solid Earth **116**.

Ferri, F., G. Di Toro, et al. (2010). "Evidence of thermal pressurization in high-velocity friction experiments on smectite-rich gouges." Terra Nova **22**(5): 347-353.

Fondriest, M., S. A. F. Smith, et al. (2013). "Mirror-like faults and power dissipation during earthquakes." Geology **41**(11): 1175-1178.

Greason, W. D. (2000). "Investigation of a test methodology for triboelectrification." Journal of Electrostatics **49**(3-4): 245-256.

Han, R. and T. Hirose (2012). "Clay-clast aggregates in fault gouge: An unequivocal indicator of seismic faulting at shallow depths?" Journal of Structural Geology **43**: 92-99.

Hector, L. G. and H. L. Schultz (1936). "The Dielectric Constant of Air at Radiofrequencies." Journal of Applied Physics **7**(4): 133-136.

Heilbronner, R. and S. Barrett (2013). Image Analysis in Earth Sciences: Microstructures and Textures of Earth Materials, Springer.

Hirose, T. and T. Shimamoto (2005). "Growth of molten zone as a mechanism of slip weakening of simulated faults in gabbro during frictional melting." Journal of Geophysical Research-Solid Earth **110**(B5).

Kim, J.-W., J.-H. Ree, et al. (2010). "Experimental evidence for the simultaneous formation of pseudotachylyte and mylonite in the brittle regime." Geology **38**(12): 1143-1146.

Kitajima, H., J. S. Chester, et al. (2010). "High-speed friction of disaggregated ultracataclasite in rotary shear: Characterization of frictional heating, mechanical behavior, and microstructure evolution." Journal of Geophysical Research-Solid Earth **115**.

Kuo, L.-W., H. Li, et al. (2014). "Gouge graphitization and dynamic fault weakening during the 2008 Mw 7.9 Wenchuan earthquake." Geology **42**(1): 47-50.

Lachenbruch, A. H. (1980). "Frictional heating, fluid pressure, and the resistance to fault motion." Journal of Geophysical Research: Solid Earth **85**(B11): 6097-6112.

Lin, A. M. (1996). "Injection veins of crushing-originated pseudotachylyte and fault gouge formed during seismic faulting." Engineering Geology **43**(2-3): 213-224.

Logan, J., M. Friedman, et al. (1979). "Experimental studies of simulated gouge and their application to studies of natural fault zones." US Geol. Surv. Open File Rep **1978**: 305-343.

Matsusaka, S., H. Maruyama, et al. (2010). "Triboelectric charging of powders: A review." Chemical Engineering Science **65**(22): 5781-5807.

Nomura, T., T. Satoh, et al. (2003). "The environment humidity effect on the tribo-charge of powder." Powder Technology **135**: 43-49.

Oohashi, K., T. Hirose, et al. (2013). "Graphite as a lubricating agent in fault zones: An insight from low ‐ to high ‐ velocity friction experiments on a mixed graphite ‐ quartz gouge." Journal of Geophysical Research: Solid Earth **118**(5): 2067-2084.

Platt, J. D., J. W. Rudnicki, et al. (2014). "Stability and localization of rapid shear in fluid ‐ saturated fault gouge: 2. Localized zone width and strength evolution." Journal of Geophysical Research: Solid Earth.

Polissar, P. J., H. M. Savage, et al. (2011). "Extractable organic material in fault zones as a tool to investigate frictional stress." Earth and Planetary Science Letters **311**(3): 439-447.

Rabinowitz, H. S., H. M. Savage, et al. (2013). "Detecting the frictional temperature rise during the 2011 Tohoku earthquake using the thermal maturity of biomarkers." Abstract T41F-07 presented at 2013 Fall Meeting, AGU, San Francisco, Calif., 9-13 Dec.

Rempe, M., T. Mitchell, et al. (2013). "Damage and seismic velocity structure of pulverized rocks near the San Andreas Fault." Journal of Geophysical Research: Solid Earth: n/a-n/a.

Rempel, A. W. and J. R. Rice (2006). "Thermal pressurization and onset of melting in fault zones." Journal of Geophysical Research: Solid Earth (1978–2012) **111**(B9).

Rietveld, H. M. (1967). "Line profiles of neutron powder-diffraction peaks for structure refinement." Acta Crystallographica **22**(1): 151-152.

Roberts, G. P. and A. M. Michetti (2004). "Spatial and temporal variations in growth rates along active normal fault systems: an example from The Lazio–Abruzzo Apennines, central Italy." Journal of Structural Geology **26**(2): 339-376.

Rowe, C. D., J. D. Kirkpatrick, et al. (2012). "Fault rock injections record paleo-earthquakes." Earth and Planetary Science Letters **335**: 154-166.

Savage, H. M., P. J. Polissar, et al. (2014). "Biomarkers heat up during earthquakes: New evidence of seismic slip in the rock record." Geology **42**(2): 99-102.

Sawai, M., T. Shimamoto, et al. (2012). "Reduction in BET surface area of Nojima fault gouge with seismic slip and its implication for the fracture energy of earthquakes." Journal of Structural Geology **38**: 117-138.

Schindelin, J., I. Arganda-Carreras, et al. (2012). "Fiji: an open-source platform for biological-image analysis." Nat Meth **9**(7): 676-682.

Sibson, R. H. (1975). "Generation of pseudotachylyte by ancient seismic faulting." Geophysical Journal International **43**(3): 775-794.

Sibson, R. H. (2003). "Thickness of the seismic slip zone." Bulletin of the Seismological Society of America **93**(3): 1169-1178.

Siman-Tov, S., E. Aharonov, et al. (2013). "Nanograins form carbonate fault mirrors." Geology **41**(6): 703-706.

Smith, S. A. F., A. Billi, et al. (2011). "Principal Slip Zones in Limestone: Microstructural Characterization and Implications for the Seismic Cycle (Tre Monti Fault, Central Apennines, Italy)." Pure and Applied Geophysics **168**(12): 2365-2393.

Smith, S. A. F., C. Collettini, et al. (2008). "Recognizing the seismic cycle along ancient faults: CO2-induced fluidization of breccias in the footwall of a sealing low-angle normal fault." Journal of Structural Geology **30**(8): 1034-1046.

Smith, S. A. F., G. Di Toro, et al. (2013). "Coseismic recrystallization during shallow earthquake slip." Geology **41**(1): 63-66.

Smith, S. A. F., G. Di Toro, et al. (2012). "Field and experimental constraints on seismic localization in granular fault gouge." Abstract S11A-06 presented at 2012 Fall Meeting, AGU, San Francisco, Calif., 3-7 Dec.

Snoke, A. W., J. Tullis, et al. (1998). Fault-related rocks: A photographic atlas, Princeton University Press.

Violay, M., S. Nielsen, et al. (2013). "Pore fluid in experimental calcite-bearing faults: Abrupt weakening and geochemical signature of co-seismic processes." Earth and Planetary Science Letters **361**: 74-84.

Warr, L. N. and S. Cox (2001). "Clay mineral transformations and weakening mechanisms along the Alpine Fault, New Zealand." Geological Society, London, Special Publications **186**(1): 85-101.

Yao, L., T. Shimamoto, et al. (2013). "Rapid postseismic strength recovery of Pingxi fault gouge from the Longmenshan fault system: Experiments and implications for the mechanisms of high‐velocity weakening of faults." Journal of Geophysical Research: Solid Earth **118**(8): 4547-4563.

8. Figure Captions

Figure 1. Summary of the occurrence of clast-cortex aggregates (CCAs) in the Tre Monti normal fault, central Italy, (a) Map of southern Italy with red lines showing the locations of the Tre Monti fault and other active normal faults that cut Holocene deposits (modified from Roberts and Michetti (2004), (b) Schematic cross-section through a segment of the Tre Monti fault showing the transition from

intact host rock to breccias and cataclasites (modified from Smith et al. (2011)). The active Quaternary fault scarp, corresponding to the principal slip surface in this fault, is marked in red. The hanging wall at the surface is composed of well-cemented Quaternary sediments, (c) scanned thin section image showing the principal slip surface and cataclastic to ultracataclastic principal slipping zone. The ultracataclasite layer closest to the principal slip surface contains well-developed CCAs. (d) Optical photomicrographs in plane-polarized light showing examples of CCAs from the ultracataclastic slipping zone of the Tre Monti fault. From left to right the CCAs increase in size and complexity. The central clasts can be composed of limestone host rock fragments (first three images) or reworked cataclastic material from the slipping zone (fourth image). In some cases, the cortex contains multiple laminations (third and fourth images and other examples in Smith et al. (2011)).

Figure 2. Experimental set-up and gouge sample holders, (a) Schematic of the ROSA rotary-shear apparatus at Padua University. (R1) and (R2): rotary encoder and potentiometer measuring revolution speed (rpm) and rotation angle, respectively. (T1) and (T2): Two compression load cells measuring the torque; output values are averaged. (D): Strain-gauge type displacement gauge measuring vertical displacement of the axial column and the experimental sample. (L): Compression load cell measuring the axial load applied to the sample via the pneumatic or hydraulic cylinders. (b) Gouge sample assembly using two solid rock cylinders and an outer Teflon ring to contain the gouge layer. The jubilee clip fastened around the Teflon sleeve is not shown in this figure. (c) Annular steel sample holder with inner and outer Teflon rings. (d) Metal sample holder used with SHIVA (modified from Smith et al., 2013). White regions: stationary parts, grey regions: rotary parts. Yellow areas show position of gouge layer contained by inner and outer metal sliding rings. Red lines demonstrate where metal parts are in sliding contact during the experiments.

Figure 3. Characterization of starting materials used in gouge experiments**,** (a) SEM images of the starting gouge material derived by crushing Carrara Marble (batch CMG 1, scale bar in inlet is 20 µm), (b) Particle size distribution of starting material derived from sieving and weighting, (c) X-ray powder diffraction spectrum for batches CMG2 (blue curve and labels) and CMG3 (black curve and labels).

Figure 4. Mechanical data from calcite gouge experiments, (a) Friction coefficient (upper three data curves) and axial displacement (lower three curves) for experiments conducted with room-dry calcite gouge. Positive changes in axial displacement indicate shortening, negative changes indicate dilation. Experiments s590 (black lines) and s776 (blue lines) performed at a normal stress of 3 MPa and slip rates of 1 and 0.1 m/s, respectively, show no weakening or transient dilation. Experiment s272 (red lines) performed at higher normal stress (17.3 MPa) at a slip rate of 0.1 m/s exhibits some weakening following peak stress after approximately 0.15 m displacement. In s272, initial gouge layer compaction is followed by transient dilation of c. 20 μm, and then renewed compaction. (b) Coefficient of friction (upper two data curves) and axial displacement (lower two data curves) for water-dampened experiments s591 (black lines; 3 MPa, 1 m/s) and s592 (blue lines; 2.8 MPa, 0.1 m/s). Neither of these experiments exhibits transient dilation or weakening.

Figure 5. Dilation vs. total displacement for experiments conducted under room-dry, wet and vacuum conditions. Transient and total (i.e. transient + secondary) dilation are plotted separately for the room-dry experiments.

Figure 6. Microstructural zones in sheared calcite gouges, (a) SEM mosaic and line drawing of room-dry experiment r88 (equivalent velocity 0.1 m/s; 1 MPa normal stress; 3 m displacement). Thin section was cut approximately halfway between edge and center of the cylindrical sample to analyze

the distribution of microstructural zones at different radial positions in the sample. Three distinct microstructural zones (Zones I-III) are recognized on the basis of grain size variations and the presence of CCAs and banding. Black boxes show the positions of b) and e). (b-e) SEM images of microstructural zones, (b) CCAs (yellow arrows) developed in Zone II. Note that the CCAs developed in a layer with relatively high porosity, (c) Close-up of CCA marked by red arrow in part b). In this example, the outer cortex is up to 10 µm wide and fine-grained materials in the cortex in-fill embayments in the central clast. Red box denotes location of d). (d) Zoom of fine-grained cortex material <1 um in size. The cortex material appears loosely aggregated, individual rounded grains down to c. 100 nm in size are recognized. (e) Anastomosing shear bands and extensive grain comminution within Zone III.

Figure 7. Strain distribution in sheared calcite gouge layers. (a) Rotary side of the steel sample holder used with SHIVA, filled with calcite gouge and prepared with two thin vertical markers of dolomite with the aid of razor blades. The starting particle size of both the calcite and the dolomite gouges in this experiment was <250 µm. Black box illustrates how post-experiment sample was cut. Sketches (modified after Scruggs and Tullis, 1998) show section though sample with unstrained and idealized strained marker assuming homogeneous strain distribution. (b) SEM mosaic and interpreted line drawing of sample s886 (3 MPa normal stress, equivalent slip velocity of 1 m/s, 2.5 m of total displacement, room-dry). The dolomite marker is distinguished by its darker grey color. The geometry of the dolomite marker broadly defines low-, intermediate- and high-strain domains. The left margin of the dolomite marker is cut by a series of R1-Riedel shears with offsets between c. 10 – 180 µm.

Figure 8. Summary of experiments performed under different conditions of slip velocity, normal stress, and ambient humidity. In the tables, **N** denotes no CCAs, **P**: poorly-developed CCAs, **W**: well-

developed CCAs (see text for definitions). Red letters denote experiments in room-dry conditions, blue letters denote water-dampened experiments. (a) Results for experiments conducted at normal stresses of 1 MPa (upper graph) and 3 MPa (lower graph), for velocities ranging from 10^{-4} - 1 m/s (log scale) and displacements ranging from 0.35 to 5.58 m. (b) Results for experiments conducted with varying normal stress and gouge layer thickness but the same target slip rate (0.1 m/s) and total displacement (3.0 m), all in room-dry conditions. (c) Results for experiments conducted in vacuum conditions with slip rates of 0.1 m/s, 3 m displacement, and variable normal stress. (d) SEM image of experimental CCAs with well-developed cortexes (experiment r89). Aggregates are abundant in this sample; most clasts with a diameter >10 µm are fully surrounded by cortexes. (e) SEM image of poorly-developed CCAs in experiment r68. In this experiment, only a few aggregates with rudimentary cortexes formed.

Figure 9. Gouge layer (experiment r91) deformed in water-saturated conditions. The microstructure of water-dampened layers is characterized by a relatively thick zone adjacent to the rotary side in which rounded to sub-rounded clasts are surrounded by a homogenously fine-grained matrix. CCAs were not identified in water-dampened experiments.

Figure 10. Grain size and shape analysis of natural and experimental CCAs, (a) The circularity of an object, in this case the central clast of a CCA, is calculated from its area and its perimeter (red dotted line) as described in the text. Solidity is calculated by dividing the area of the object (red dotted line) by the convex area having no embayments (black dotted line). (b) SEM image (left) and corresponding tracing (right) of experimental sample r80 containing well-developed CCAs (n = 45). In the tracing, red grains are central clasts, grey areas are outer cortexes. (c) Optical photomicrograph mosaic (upper image) and corresponding tracing (lower image) of natural CCAs (n = 137) from the

principal slip zone of the Tre Monti fault. The box shows the area of the photomicrograph mosaic. In the tracing, red grains are central clasts, grey areas are outer cortexes.

Figure 11. Results of quantitative analysis of circularity (a) and solidity (b) of samples shown in Figure 10. Bin sizes were chosen to reveal differences in the data and are 0.1 for circularity and 0.025 for solidity.

Figure 12. Examples of experimental CCAs from sample r80, (a) Rounded grain composed of reworked matrix material and lacking a central clast, (b) CCA consisting of two laminations (yellow arrows) surrounding a central clast. Note that in both of the images some of the smaller grains are also CCAs (red arrows).

9. Tables

Table 1. Summary of naturally-occurring CCAs in tectonic fault zones and landslides. Modified after Han and Hirose (2012).

Table 2. Summary of experimental conditions, dilation measurements, and classification of CCAs.

Table 1: Summary of naturally-occurring CCAs in tectonic fault zones and landslides. Modified after Han and Hirose (2012).

Location	Setting	CCA host rock composition	Formation /Exhumation Depth	Evidence of fluids	Reference
Tre Monti fault, Italy	Normal fault	Fossiliferous and micritic limestone	<2 km	Evidence of layer fluidization and syn-tectonic vein formation	Smith et al. (2011)
Alpine fault, New Zealand	Strike-slip fault	Mylonite-derived clay-gouge	2-4 km (attributed to the depth of growth of swelling clays)	Hydrous chloritization, dissolution, fluid-induced sub-critical cracking	Warr and Cox (2001)
Chelungpu fault, Taiwan	Thrust fault	Clay-rich gouge	1.11-1.14 km	Evidence for gouge layer fluidization	Boullier et al. (2009)
Palisades slide block, USA	Landslide	Basal layer where lithologies of upper plate (limestones) and lower plate (sandstone-conglomerate-like rock with clayey matrix) mix	<250 m	No evidence for or against involvement of fluids	Anders et al. (2000), Boyer and Hossack (1992)
Heart Mountain, WY, MT, USA	Landslide	Dolomite	2-4 km	Evidence for fluidization either with or without water	Beutner and Craven (1996), Beutner and Gerbi (2005), Anders et al. (2010)

Table 1

824

Table 2: Summary of experimental conditions, dilation measurements, and classification of CCAs.

	Name	wt% H_2O	σ_n (MPa)	v_e (m/s)[a]	d_e (m)[b]	Sample holder	Starting material batch	Gouge layer thickness (mm)	Net axial displacement (μm)[c]	Transient dilation (μm)	Total dilation	Aggregates
Room-Humidity conditions	r103	0	1	0.0001	3.05	Gabbro	CMG2	1.5	250	7	75	**W**
	r69	0	1	0.001	0.62	Steel	CMG1	1.5	20	0	26	N
	r78	0	1	0.001	0.64	Steel	CMG1	4.3	730	0	0	N
	r93	0	1	0.001	3	Gabbro	CMG2	1.8	30	7	108	**W**
	r89	0	1	0.001	5.05	Rock	CMG2	2.1	-80	120	175	**W**
	r68	0	1	0.1	0.53	Steel	CMG1	1.5	290	0	0	P
	r73	0	1	0.1	0.53	Steel	CMG1	0.36	70	0	0	P
	r88	0	1	0.1	3	Rock	CMG1	1.5	300	7	15	**W**
	r80	0	1	0.1	5	Tonalite	CMG1	1.5	250	23	28	**W**
	r82	0	1	1	5	Tonalite	CMG1	1.5	380	13	17	**W**
	r71	0	3	0.001	0.65	Steel	CMG1	1.5	270	0	0	N
	r105	0	3	0.001	5	Gabbro	CMG2	1.5	120	0	70	**W**
	r70	0	3	0.1	0.54	Steel	CMG1	0.9	105	0	0	N
	s787	0	3	0.1	2.72	SHiVA	CMG2		100	20	60	P
	r85	0	3	0.1	3	Tonalite	CMG1	1.5	1140	15	41	P
	s776	0	3	0.1	3.35	Shiva	CMG2	3	100	140	140	N
	r90	0	3	0.1	3.85	Gabbro	CMG2	1.7	120	9	38	**W**
	s775	0	3	0.1	5.58	SHiVA	CMG2	1.8	230	90	90	P
	s590	0	3	1	0.5	SHiVA	CMG1	3	280	0	0	N
	r86	0	3	1	1.9	Tonalite	CMG1	1.7	220	0	0	P
	s777	0	3	1	2.5	SHiVA	CMG2	1.8	60	14	14	P
	s886	0	3	1	2.5	SHiVA	<250 μm	3	125	27	26.614	N

	s778	0	5	0.1	3	SHiVA	CMG2	3	90	60	113.4	**W**
	s811	0	10	0.1	2.25	SHiVA	CMG2	3	100	20	40	P
	s272	0	17.3	0.1	1.15	SHiVA	CMG3	3	280	19	19.42	N
Water-dampened	r92	22	1	0.001	4.45	Gabbro	CMG2	1.8	400	0	0	N
	r74	20	1	0.1	0.65	Steel	CMG1	0.4	360	0	0	N
	r91	25	1	0.1	4	Rock	CMG2	1.6	200	0	20	N
	r83	20	1.6	0.0005	0.27	Tonalite	CMG1	1.8	170	0	0	N
	s592	~15	2.8	0.1	0.5	SHiVA	CMG1	3	185	0	0	N
	r84	20	3	0.001	0.5	Tonalite	CMG1	1.5	640	0	0	N
	r72	40	3	0.1	>0.5	Steel	CMG1	1.5	-	0	0	N
	s591	20	3	1	0.5	SHiVA	CMG1	3	320	0	0	N
											0	
Vacuum	s812	0	3	0.1	1.93	SHiVA	CMG3	3	160	10	50	N
	s813	0	5	0.1	3.35	SHiVA	CMG3	3	220	0	0	P
	s814	0	10	0.1	2.79	SHiVA	CMG3	3	360	0	0	N

[a]equivalent velocity, [b]equivalent displacement, see text for definitions. [c]positive value: net compaction, negative value: net dilation

Table 2

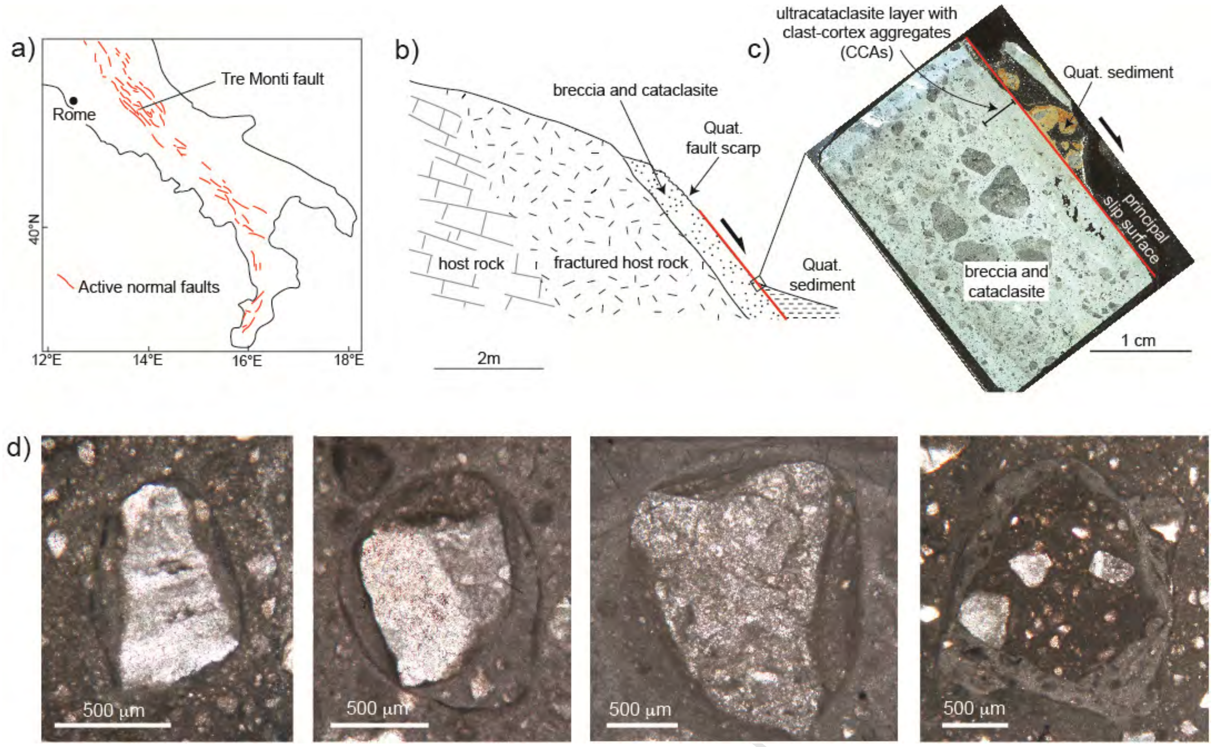
a)
Tre Monti fault
Rome
40°N
Active normal faults
12°E
14°E
16°E
18°E
b)
breccia and cataclasite
Quat. fault scarp
host rock
fractured host rock
Quat. sediment
2m
c)
ultracataclasite layer with clast-cortex aggregates (CCAs)
Quat. sediment
principal slip surface
breccia and cataclasite
1 cm
d)
500 μm
500 μm
500 μm
500 μm

Figure 1

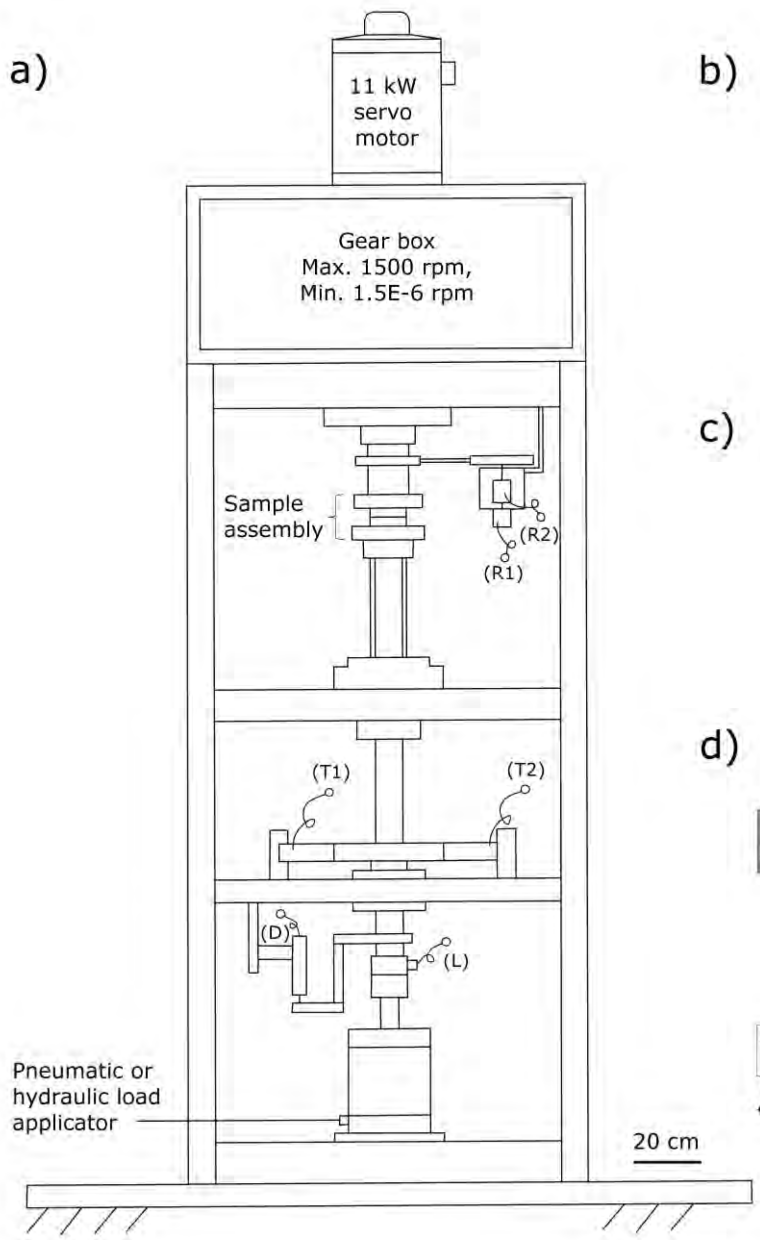

a)
11 kW
servo
motor
Gear box
Max. 1500 rpm,
Min. 1.5E-6 rpm
Sample
assembly
(R2)
(R1)
(T1)
(T2)
(D)
(L)
Pneumatic or
hydraulic load
applicator
20 cm
b)
25 mm
Rock
cylinder
Gouge
layer
Teflon
sleeve
c)
Teflon rings
Gouge
layer
Steel
parts
25 mm
d)
Base disc
Outer ring
Inner ring
Spring
130 mm

Figure 2

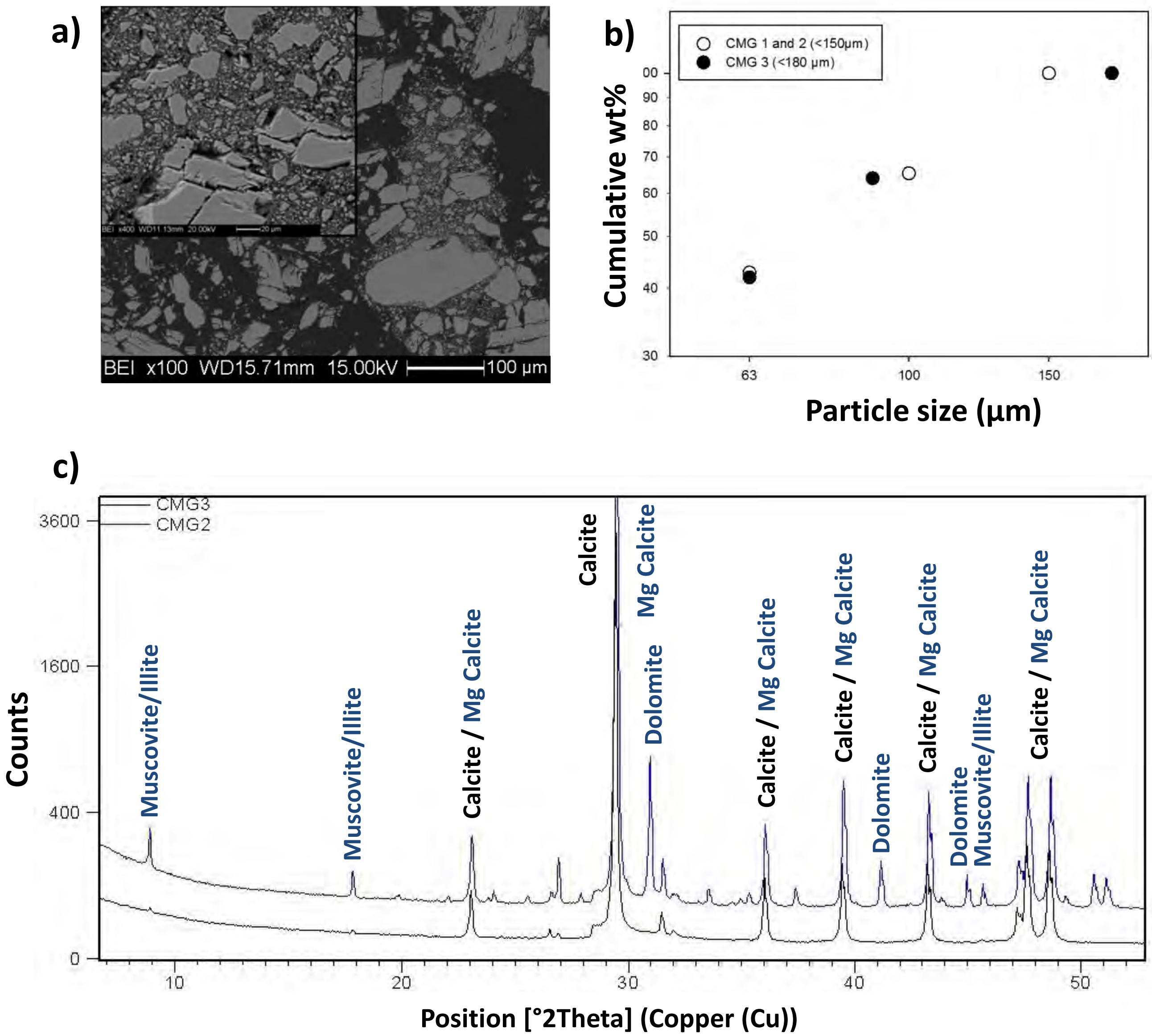
a)
BEI x100 WD15.71mm 15.00kV 100 µm
b)
CMG 1 and 2 (<150µm)
CMG 3 (<180 µm)
Cumulative wt%
00
90
80
70
60
50
40
30
63
100
150
Particle size (µm)
c)
CMG3
CMG2
3600
1600
400
0
Counts
Muscovite/Illite
Muscovite/Illite
Calcite / Mg Calcite
Calcite
Mg Calcite
Dolomite
Calcite / Mg Calcite
Calcite / Mg Calcite
Dolomite
Calcite / Mg Calcite
Dolomite
Muscovite/Illite
Calcite / Mg Calcite
10
20
30
40
50
Position [°2Theta] (Copper (Cu))

Figure 3

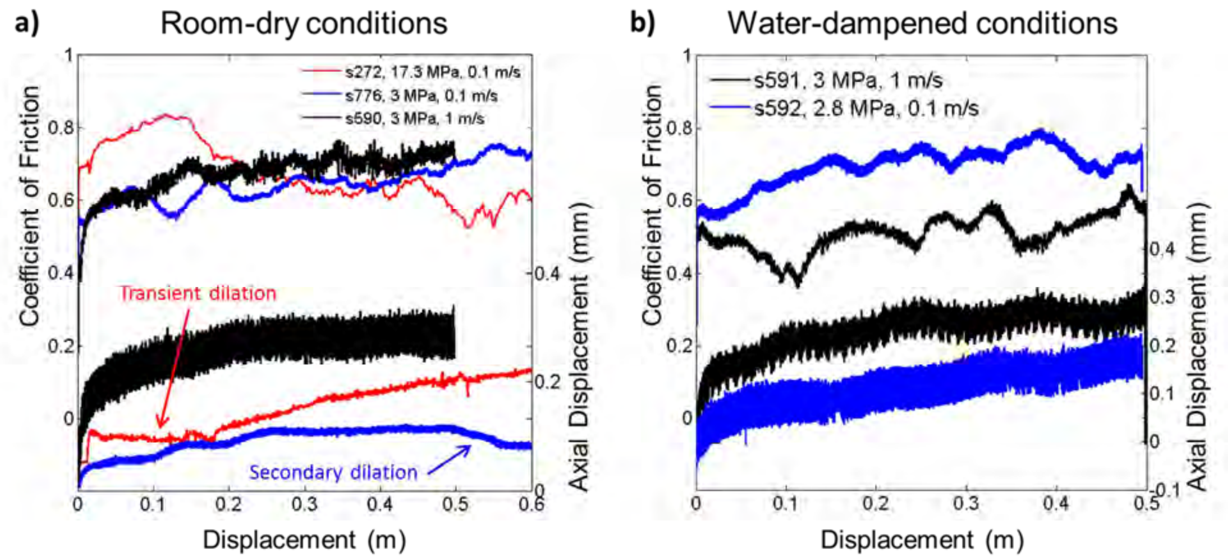

a)
Room-dry conditions
s272, 17.3 MPa, 0.1 m/s
s776, 3 MPa, 0.1 m/s
s590, 3 MPa, 1 m/s
Coefficient of Friction
Axial Displacement (mm)
Transient dilation
Secondary dilation
Displacement (m)
b)
Water-dampened conditions
s591, 3 MPa, 1 m/s
s592, 2.8 MPa, 0.1 m/s
Coefficient of Friction
Axial Displacement (mm)
Displacement (m)

Figure 4

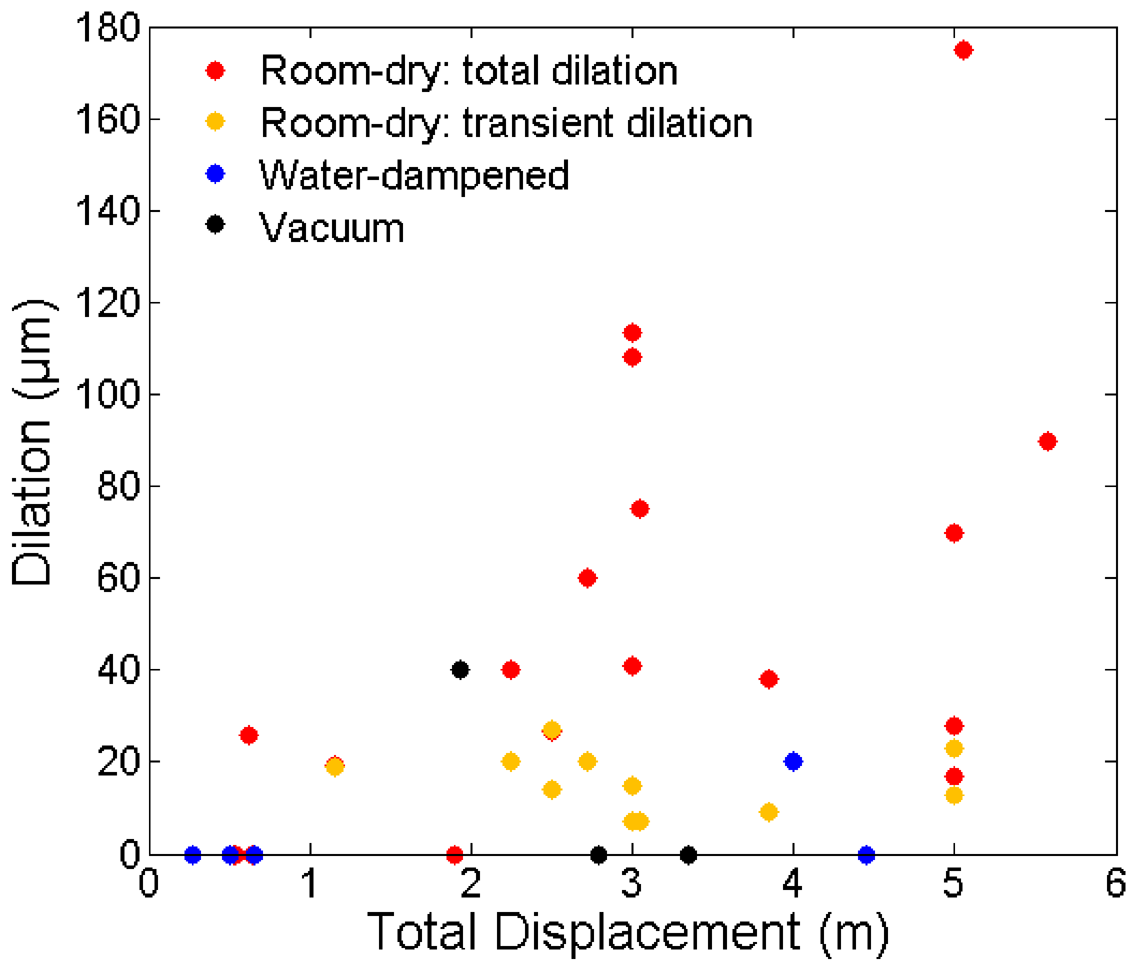

Room-dry: total dilation
Room-dry: transient dilation
Water-dampened
Vacuum
Dilation (µm)
Total Displacement (m)
0
20
40
60
80
100
120
140
160
180
0
1
2
3
4
5
6

Figure 5

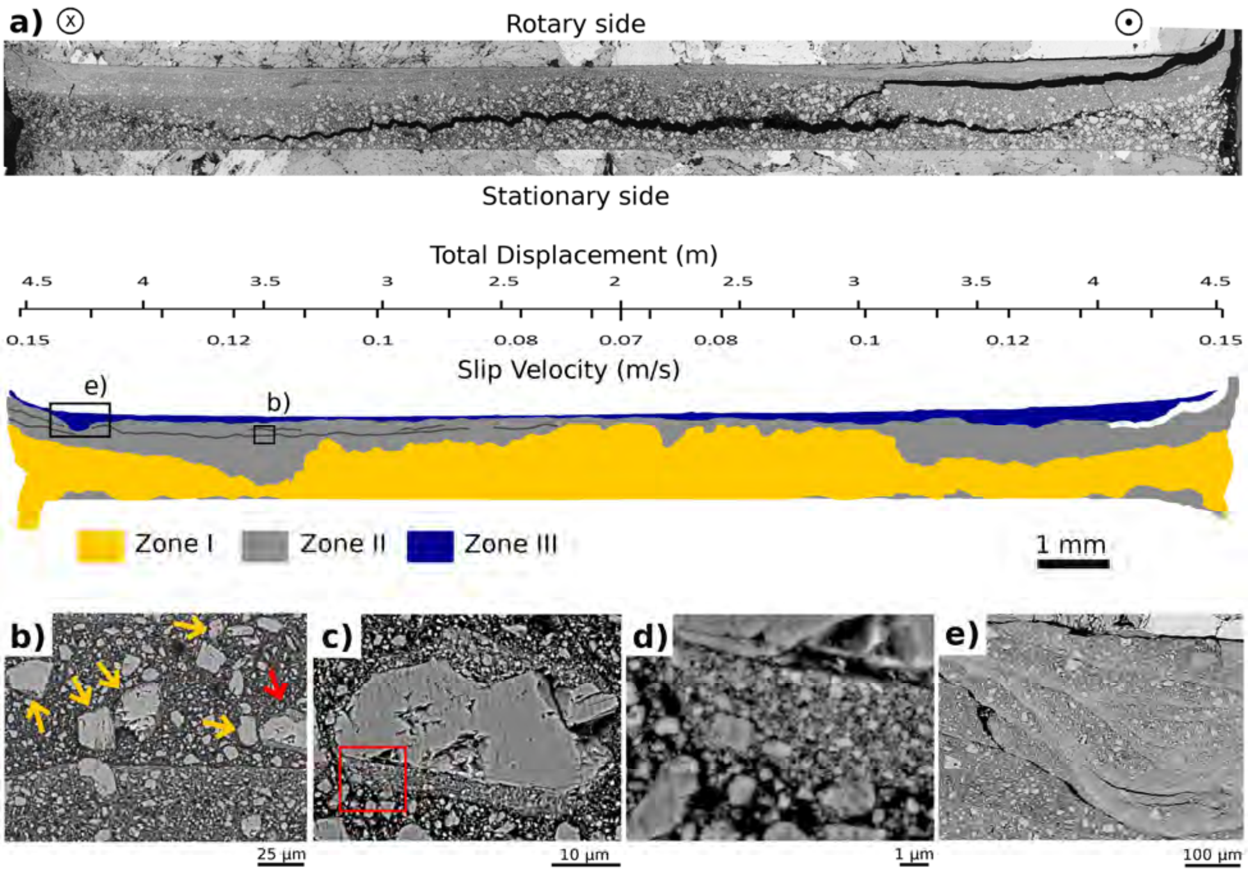
a)
Rotary side
Stationary side
Total Displacement (m)
4.5
4
3.5
3
2.5
2
2.5
3
3.5
4
4.5
0.15
0.12
0.1
0.08
0.07
0.08
0.1
0.12
0.15
Slip Velocity (m/s)
e)
b)
Zone I
Zone II
Zone III
1 mm
b)
c)
d)
e)
25 µm
10 µm
1 µm
100 µm

Figure 6

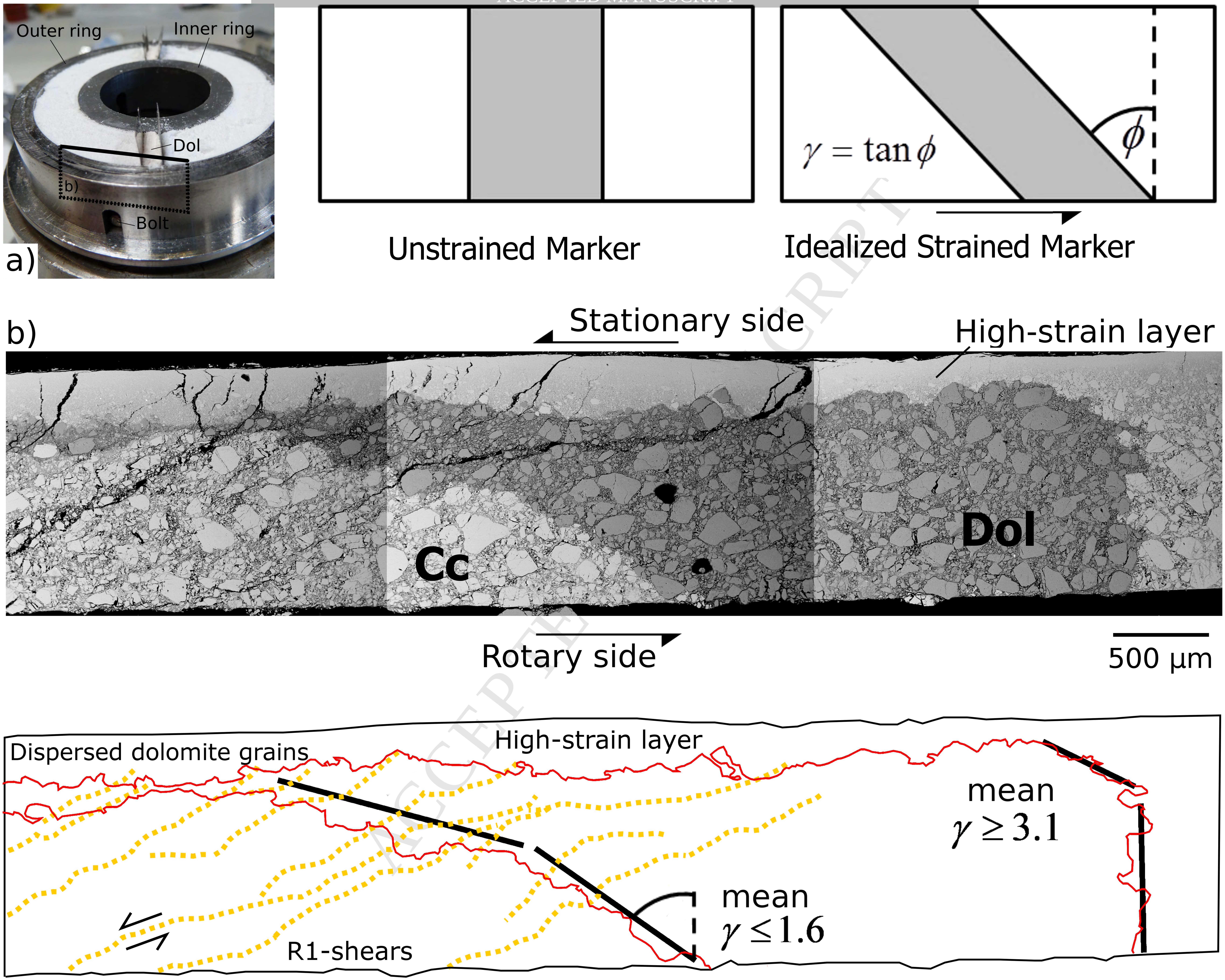

a)
Outer ring
Inner ring
Dol
b)
Bolt
Unstrained Marker
$\gamma = \tan\phi$
ϕ
Idealized Strained Marker
b)
Stationary side
High-strain layer
Cc
Dol
Rotary side
500 µm
Dispersed dolomite grains
High-strain layer
mean $\gamma \geq 3.1$
mean $\gamma \leq 1.6$
R1-shears

Figure 7

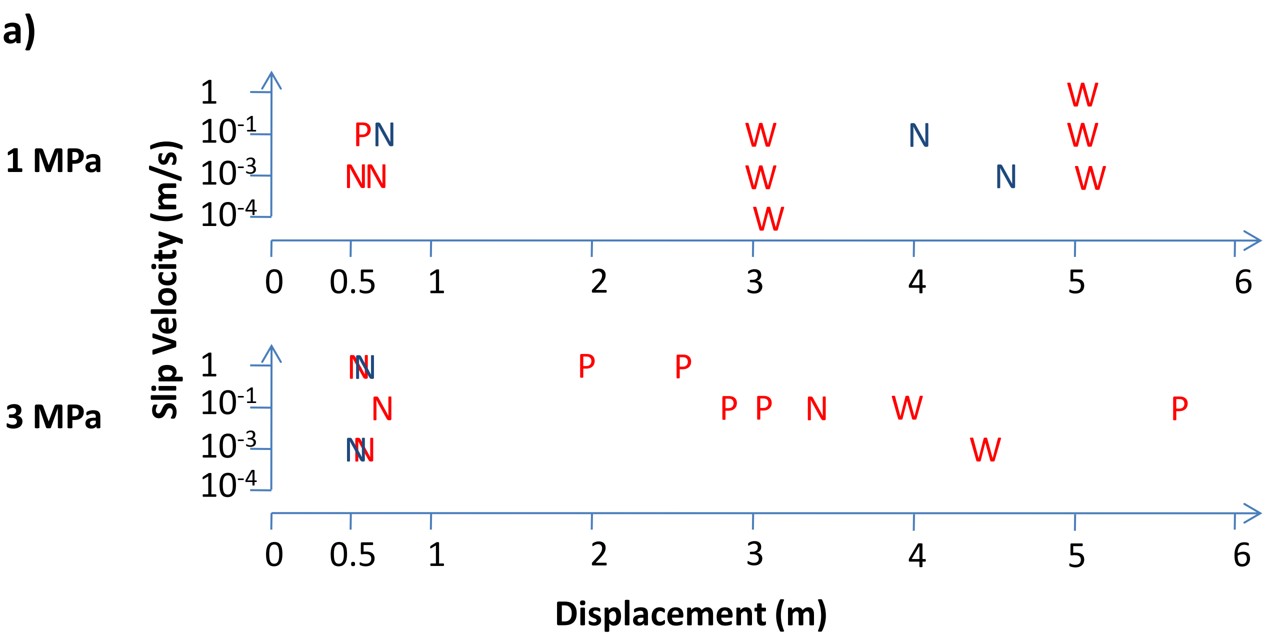

b)

σ_n (MPa)	Gouge layer (mm)	Aggregates
1	1.5	W
3	1.5	P
5	3	W
10	3	P
17	3	N

c)

σ_n (MPa)	Gouge layer (mm)	Aggregates
3	3	N
5	3	P
10	3	N

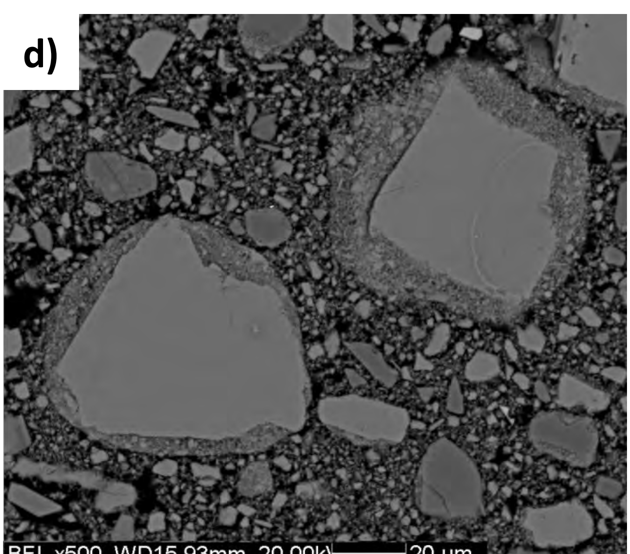

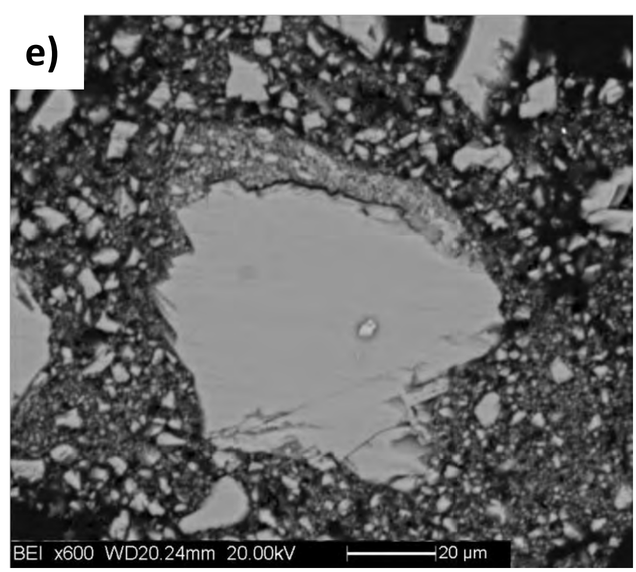

Figure 8

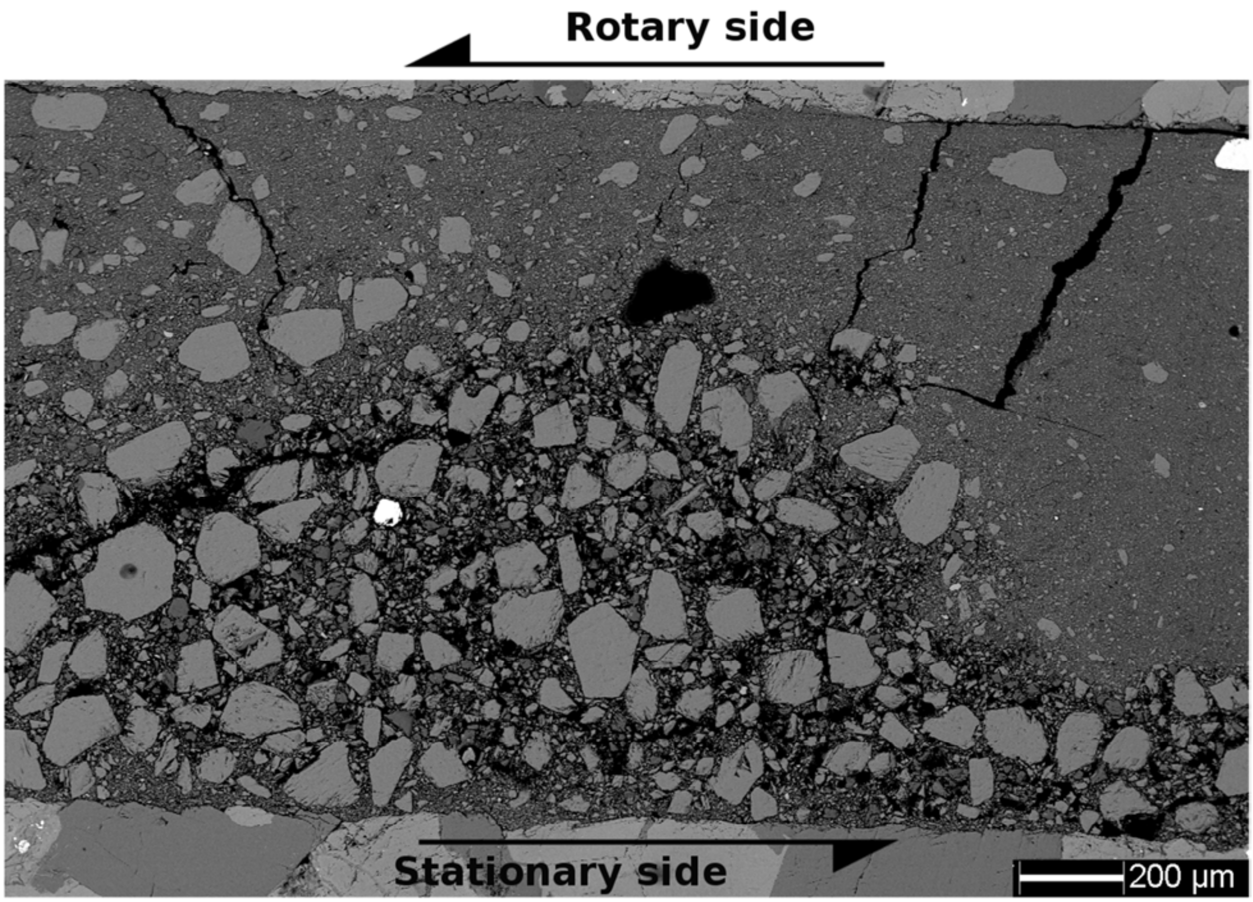

Figure 9

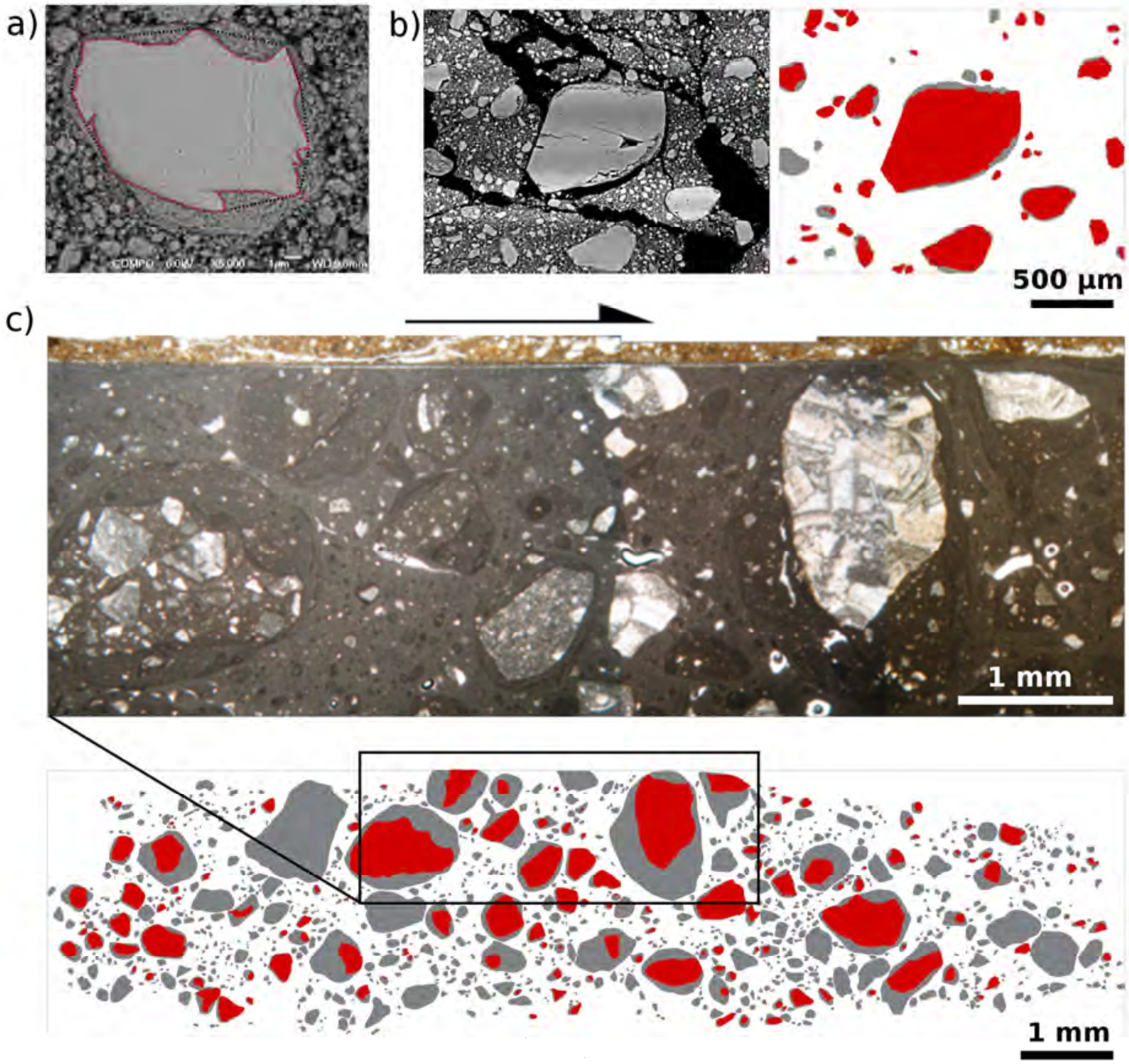

Figure 10

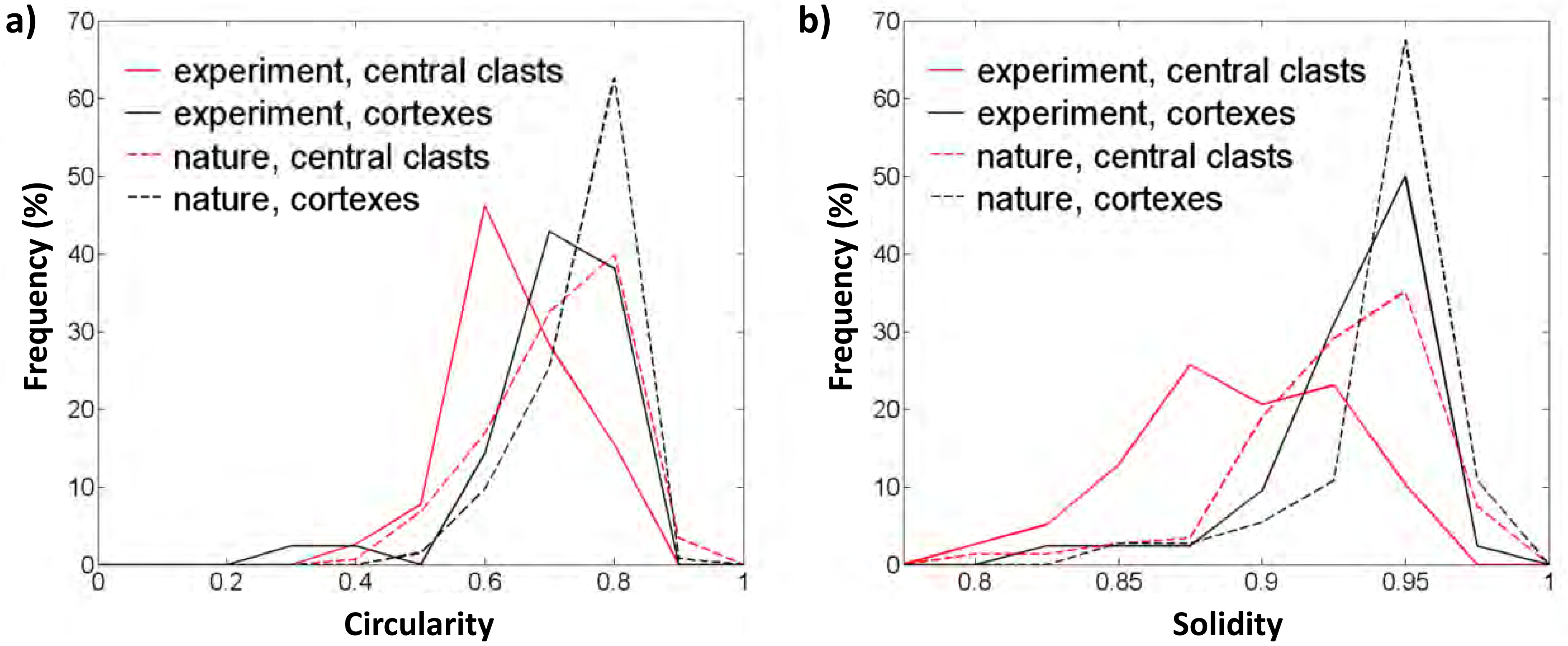
a)
b)
experiment, central clasts
experiment, cortexes
nature, central clasts
nature, cortexes
Frequency (%)
Circularity
Solidity
0
10
20
30
40
50
60
70
0
0.2
0.4
0.6
0.8
1
0.8
0.85
0.9
0.95
1

Figure 11

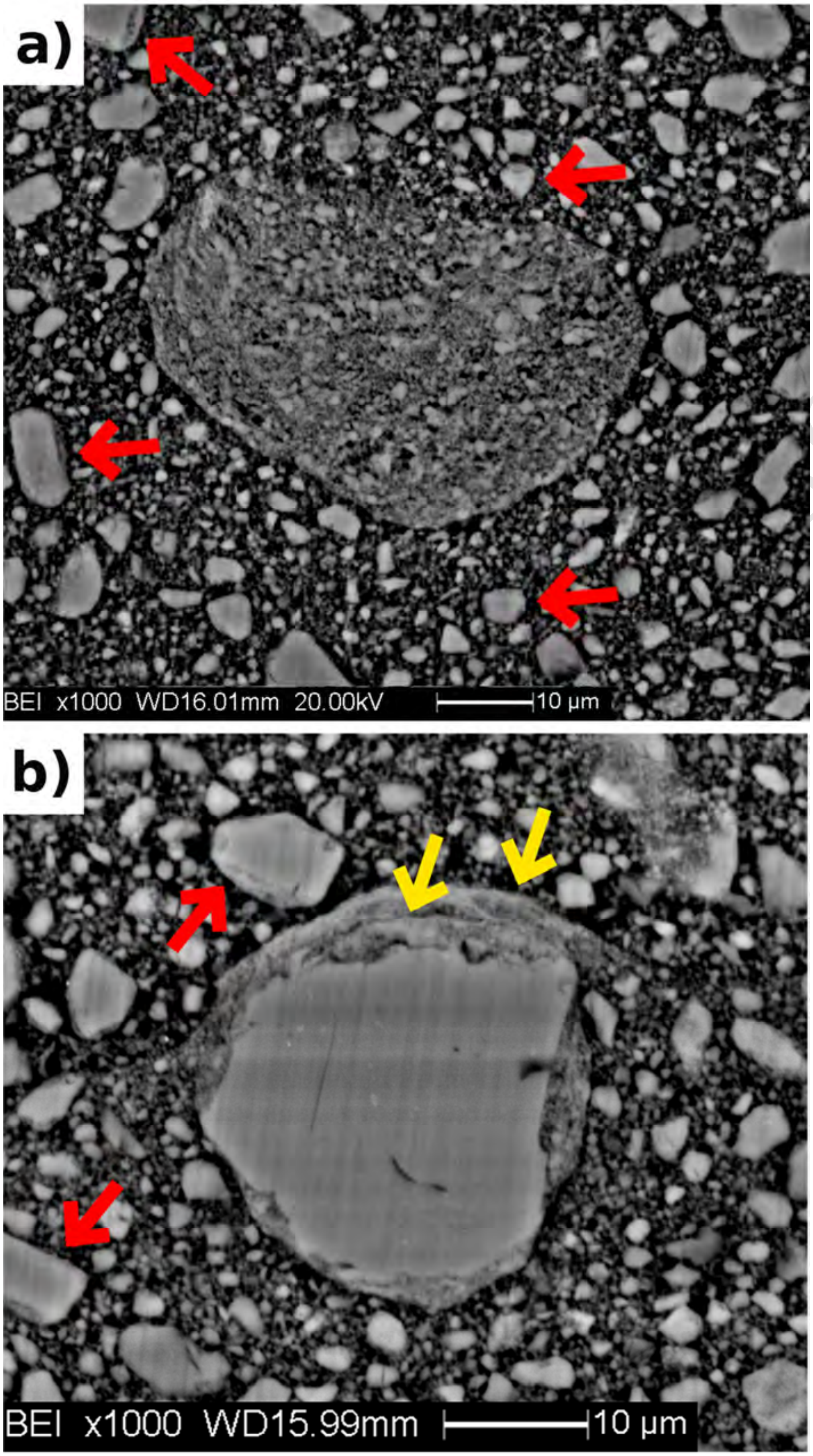

Figure 12

Highlights

"Clast-cortex aggregates in experimental and natural calcite-bearing fault zones", Rempe et al.

- Clast-cortex aggregates (CCAs) produced experimentally in calcite gouges
- Favored by low normal stresses and room-dry conditions
- Developed at all investigated slip rates (0.001 m/s to 1 m/s)
- Formation by grain rolling and accretion at intermediate strains
- CCAs not a reliable indicator of seismic slip in fault zones